SUBMILLIMETER OBSERVATIONS OF GIANT MOLECULAR CLOUDS IN THE LARGE MAGELLANIC CLOUD: TEMPERATURE AND DENSITY AS DETERMINED FROM $J = 3–2$ AND $J = 1–0$ TRANSITIONS OF CO

Tetsuhiro Minamidani,[1,2] Norikazu Mizuno,[1] Yoji Mizuno,[1] Akiko Kawamura,[1] Toshikazu Onishi,[1] Tetsuo Hasegawa,[3] Ken'ichi Tatematsu,[3] Masafumi Ikeda,[4] Yoshiaki Moriguchi,[1] Nobuyuki Yamaguchi,[3] Jürgen Ott,[5,6] Tony Wong,[7,8] Erik Muller,[7] Jorge L. Pineda,[9] Annie Hughes,[7,10] Lister Staveley-Smith,[11] Ulrich Klein,[9] Akira Mizuno,[1,12] Silvana Nikolić,[13,14] Roy S. Booth,[13,15] Arto Heikkilä,[13] Lars-Åke Nyman,[16] Mikael Lerner,[16] Guido Garay,[17] Sungeun Kim,[18] Motosuji Fujishita,[1] Tokuichi Kawase,[1] Monicá Rubio,[17] and Yasuo Fukui[1]

ABSTRACT

We have carried out submillimeter ^{12}CO($J = 3–2$) observations of six giant molecular clouds (GMCs) in the Large Magellanic Cloud (LMC) with the ASTE 10 m submillimeter telescope at a spatial resolution of 5 pc and very high sensitivity. We have identified 32 molecular clumps in the GMCs and revealed significant details of the warm and dense molecular gas with $n(H_2) \sim 10^3$–10^5 cm^{-3} and $T_{kin} \sim 60$ K. These data are combined with ^{12}CO($J = 1–0$) and ^{13}CO($J = 1–0$) results and compared with LVG calculations. The results indicate that clumps that we detected are distributed continuously from cool ($\sim$10–30 K) to warm ($\gtrsim$30–200 K), and warm clumps are distributed from less dense ($\sim 10^3$ cm^{-3}) to dense ($\sim 10^{3.5}$–10^5 cm^{-3}). We found that the ratio of ^{12}CO($J = 3–2$) to ^{12}CO($J = 1–0$) emission is sensitive to and is well correlated with the local Hα flux. We infer that differences of clump properties represent an evolutionary sequence of GMCs in terms of density increase leading to star formation. Type I and II GMCs (starless GMCs and GMCs with H II regions only, respectively) are at the young phase of star formation where density does not yet become high enough to show active star formation, and Type III GMCs (GMCs with H II regions and young star clusters) represent the later phase where the average density is increased and the GMCs are forming massive stars. The high kinetic temperature correlated with Hα flux suggests that FUV heating is dominant in the molecular gas of the LMC.

Subject headings: galaxies: individual (LMC) — ISM: clouds — ISM: molecules — Magellanic Clouds — radio lines: ISM — submillimeter

Online material: color figures

1. INTRODUCTION

It is of fundamental importance in astronomy to understand the evolution of galaxies. Since a major constituent of galaxies is stars, the formation of stars is a fundamental process in galactic evolution. The properties of stars characterize the basic contents of galaxies and their time evolution. We understand from studies of the Milky Way that giant molecular clouds (GMCs), whose mass ranges from 10^5 to 10^7 $M_\odot$, are the principal sites of star formation and that this perhaps holds true in other galaxies as well. We also recognize that the GMC properties (e.g., L_{CO}–line width relation, index of mass spectrum) are similar among five galaxies in the Local Group according to the spatially resolved studies (Blitz et al. 2007). This supports the idea that studies of GMCs will be useful in understanding the fundamentals of galactic evolution through the formation and evolution of GMCs and star formation therein.

Observational studies of GMCs have been most effectively made by the millimeter interstellar carbon monoxide emission line at 2.6 mm, which allows us to probe molecular gas whose density is greater than $\sim$100 cm^{-3}. We note that the most abundant species, molecular hydrogen, does not have appropriate line emissions in the millimeter and submillimeter region due to its zero permanent electric dipole moment and large separation between

[1] Department of Astrophysics, Nagoya University, Furo-cho, Chikusa-ku, Nagoya 464-8602, Japan.
[2] Current address: Department of Physics, Faculty of Science, Hokkaido University, N10W8, Kita-ku, Sapporo 060-0810, Japan.
[3] National Astronomical Observatory of Japan, Mitaka, Tokyo 181-8588, Japan.
[4] Research Center for the Early Universe and Department of Physics, University of Tokyo, Tokyo 113-0033, Japan.
[5] National Radio Astronomy Observatory, 520 Edgemont Road, Charlottesville, VA 22903-2475.
[6] Jansky Fellow of the National Radio Astronomy Observatory.
[7] CSIRO Australia Telescope National Facility, P.O. Box 76, Epping, NSW 1710, Australia.
[8] Current address: Department of Astronomy, MC 221, University of Illinois, Urbana, IL 61801.
[9] Radioastronomisches Institut der Universität Bonn, Auf dem Hügel 71, 53121 Bonn, Germany.
[10] Center for Supercomputing and Astrophysics, Swinburne University of Technology, Hawthorn, VIC 3122, Australia.
[11] School of Physics, M013, University of Western Australia, 35 Stirling Highway, Crawley, WA 6009, Australia.
[12] Current address: Solar-Terrestrial Environment Laboratory, Nagoya University, Furo-cho, Chikusa-ku, Nagoya 464-8601, Japan.
[13] Onsala Space Observatory, 439-92 Onsala, Sweden.
[14] Current address: Departament de Astronomía, Universidad de Chile, Casilla 36-D, Santiago, Chile.
[15] Current address: Hartebeesthoek Radio Astronomy Observatory, P.O. Box 443, Krugersdorp 1740, South Africa.
[16] European Southern Observatory, Casilla 19001, Santiago 19, Chile.
[17] Departament de Astronomía, Universidad de Chile, Casilla 36-D, Santiago, Chile.
[18] Astronomy and Space Science Department, Sejong University, 98 Kwangjin-gu, Kunja-dong, Seoul 143-747, Korea.

the lowest energy levels, which are not excited significantly in the typical physical conditions of molecular clouds.

Recent advances in submillimeter observations have allowed us to determine physical parameters of molecular clouds over much larger ranges than in the millimeter region by comparing line intensities between different transitions. These submillimeter studies were initiated by the Swedish-ESO Submillimetre Telescope (SEST) 15 m telescope in Chile followed by instruments in Mauna Kea, Hawaii, and in the Swiss Alps at an altitude range from 3700 to 4200 m, including the Caltech Submillimeter Observatory (CSO) 10 m, James Clerk Maxwell Telescope (JCMT) 15 m, and KOSMA 3 m telescopes, and the Antarctic Submillimeter Telescope and Remote Observatory (AST/RO) 1.6 m telescope in Antarctica. Subsequently, in the 2000s, the development of new instruments at an altitude of $\sim$5000 m in Atacama in northern Chile resulted in a superior capability because of the high altitude and dry characteristics of the site. The instruments installed in Atacama include the Atacama Submillimeter Telescope Experiment (ASTE) 10 m, APEX 12 m, and NANTEN2 4 m telescopes. All these instruments are beginning to take new molecular data with significantly better quality than before in terms of noise level, as well as angular resolution. It is also noteworthy that the current frequency coverage extends as high as the 800 GHz band and even the terahertz region.

Among nearby galaxies that we can observe at reasonably high spatial resolutions, the Large and Small Magellanic Clouds offer us a unique opportunity to achieve the highest resolutions due to their unrivaled closeness, 50–60 kpc. In particular, the Large Magellanic Cloud (LMC) is actively forming stars in clusters and is an ideal laboratory for us to study star formation, particularly massive star formation in star clusters. In the LMC, the metallicity is a factor of $\sim$3 lower than in the solar neighborhood (Dufour et al. 1982; Dufour 1984; Rolleston et al. 2002). In addition, the visual extinctions are lower and the FUV field is stronger in the LMC than in the Milky Way (Israel et al. 1986), characterizing the initial conditions of star formation.

The first spatially resolved complete sample of GMCs in a single galaxy has been obtained toward the whole LMC with the NANTEN 4 m telescope in 2.6 mm CO emission at 40 pc resolution (Fukui et al. 1999, 2001, 2007; Mizuno et al. 2001). These studies revealed the three types of GMCs in terms of star formation activities; type I is starless, type II is with H II regions only, and type III is associated with active star formation indicated by huge H II regions and young star clusters, where the stars identified are only O stars due to the sensitivity limitation. It also revealed that the lifetime of a GMC is as short as $\sim$30 Myr (Fukui 2007; Kawamura et al. 2007; A. Kawamura et al. 2008, in preparation). These previous studies naturally place the LMC as one of the prime targets for submillimeter studies to derive the physical parameters of GMCs.

Another aspect that deserves our attention is that very young, rich stellar clusters are forming in the LMC. These are so-called populous clusters, which are very rare in the Milky Way and resemble globular clusters formed in the primeval Milky Way. The open clusters forming in the Milky Way are small in the number of stars and loose in spatial distribution. Along with the low metallicity of the LMC, it is an interesting possibility to use molecular data to investigate the formation mechanism of super star clusters at the molecular cloud stage.

In the past, there have been some studies that used the higher transitions ($J = 2$–$1, J = 3$–$2, J = 4$–$3, J = 7$–6) of CO spectra of the molecular clouds in the LMC (e.g., Sorai et al. 2001; Johansson et al. 1998; Heikkilä et al. 1999; Bolatto et al. 2005; Israel et al. 2003; Kim et al. 2004; Kim 2006). These studies suggest that the molecular gas may be warmer and/or denser than in the Milky Way.

Johansson et al. (1998) used the SEST 15 m telescope to observe the central part of the 30 Doradus Nebula (rms $\sim$0.2 K at 0.5 km s^{-1} velocity resolution for $J = 1$–0 and rms $\sim$1.0 K at 0.5 km s^{-1} velocity resolution for $J = 3$–2) and the southern H II regions N158C, N159, and N160 with a few prominent CO clouds in the $J = 2$–1 and $J = 3$–2 transitions of CO. They find that the kinetic temperatures are 10–80 K and the highest temperature is toward 30 Dor. The smallest beam size and grid spacing are 15″ and 11″, respectively, in the $J = 3$–2 emission. Heikkilä et al. (1999) used SEST to observe the $J = 3$–2 transition of CO in N159 and 30 Doradus, as well as other rarer molecular species. This study aimed at obtaining chemical abundances, while it also provides more information on cloud temperature, etc., from CO($J = 3$–2) data. The kinetic temperatures that they derived are 50 K in 30 Dor-10, 15 K in 30 Dor-27, and 20–25 K in N159W and N160. Bolatto et al. (2005) employed the AST/RO to observe the ^{12}CO($J = 4$–3) transition at 461 GHz with a 109″ beam. They observed nine regions in the LMC at $6' \times 6'$ field, all with H II regions, and derived kinetic temperatures from a comparison between the CO($J = 4$–3) and ($J = 1$–0) transitions. N48, N55A, N79, N83A, N113, N159W, N167, N214C, and LIRL 648 are included. They derive temperatures of 100–300 K and note a trend that higher temperatures occur in moderate-density regions, 100–1000 cm^{-3}, and the lower temperatures in much denser regions, 10^4–10^5 cm^{-3}. These studies were preceded by a suggestion that significant amounts of warm molecular gas may exist in the LMC (Israel et al. 2003). Kim et al. (2004) also made similar observations toward an H II region, N44, and suggest very dense gas of $\sim 10^5$ cm^{-3}. Most recently, Kim (2006) derived $T_{\rm kin} = 100$ K and $n \sim 10^{4.3}$ cm^{-3} for 30 Dor from the intensity ratios of ^{12}CO($J = 7$–6) to ^{12}CO($J = 4$–3) and ^{12}CO($J = 1$–0) to ^{13}CO($J = 1$–0).

In the present study, we aim to obtain submillimeter molecular data at better signal-to-noise ratios than in the previous studies to make estimates of temperatures and densities over a large sample in the LMC. We combine the ^{12}CO($J = 3$–2) data obtained with the ASTE telescope and CO($J = 1$–0) data obtained with the SEST and Mopra telescopes. In order to make reasonable comparisons between the two transitions, $J = 3$–2 and $J = 1$–0, we smooth the ASTE results (22″ beam) to the same resolution as the SEST data (45″) and use large velocity gradient (LVG) calculations to estimate density and temperature. We also employ the ^{13}CO($J = 1$–0) data, where available, to place constraints on the physical parameters.

This paper is organized as follows: § 2 describes the observations. Sections 3 and 4 show the results and data analysis, respectively. In § 5, we discuss the physical properties of clumps and evolutional sequence of GMCs. Finally, we present a summary in § 6.

2. OBSERVATIONS

2.1. *Selection of GMCs*

The present targets were chosen from the NANTEN catalog of ^{12}CO($J = 1$–0) GMCs compiled by Fukui et al. (2007). This catalog is based on the second survey, with a factor of $\sim$2 higher sensitivity than the first survey (Mizuno et al. 2001). The catalog includes 272 CO clouds, 230 of which are detected at three or more observed positions, and they are classified into the three types: 56 (24.3%) type I (starless) GMCs, 120 (52.2%) type II GMCs (those with H II regions only), and 54 (23.5%) type III GMCs (those with H II regions and young star clusters), where "stars"

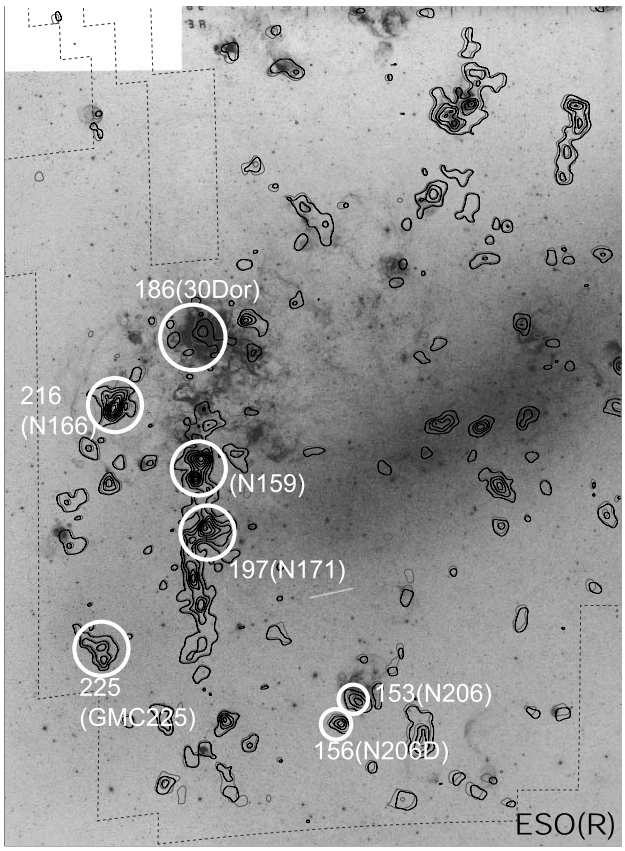

FIG. 1.— CO velocity-integrated intensity map (Fukui et al. 2001, 2007) overlaid on ESO(R) image. The observed seven regions are indicated by white circles. [*See the electronic edition of the Supplement for a color version of this figure.*]

refer only to O stars due to the limited sensitivity of existing observations (A. Kawamura et al. 2008, in preparation; Fukui 2007; Kawamura et al. 2007; Blitz et al. 2007).

Among these GMCs, we mainly focus on type III GMCs whose ^{12}CO($J = 3$–2) intensities are expected to be strong due to the highly excited conditions. In addition, relatively high resolution ^{12}CO and ^{13}CO $J = 1$–0 data, observed with the SEST 15 m or Mopra 22 m telescopes, are collected to derive physical properties of molecular clouds through the LVG analysis at a 10 pc scale.

In the present study, we observe GMCs in the southeast region of the LMC, which contains 30 Doradus, the largest and most massive H II region in the Local Group. We observe the molecular ridge extending southward from 30 Doradus and the "CO Arc" along the southeastern optical edge (Fukui et al. 1999). Three type III GMCs, LMC N J0538−6904 (the 30 Dor region), LMC N J0540−7008 (the N159 region and the N171 region), and LMC N J0530−7106 (the N206 region), are selected as the principal targets, and two type II GMCs, LMC N J0544−6923 (the N166 region) and LMC N J0532−7114 (the N206D region), and a type I GMC, LMC N J0547−7041 (the GMC 225 region), are included for reference. The locations of the observed GMCs and regions are shown in Figure 1, and their coordinates and the data used in this paper are summarized in Table 1. Hereafter, the region names, which are in the parentheses above or column (4) of Table 1, are used to identify the regions.

2.2. ^{12}CO($J = 3$–2)

Observations of the ^{12}CO($J = 3$–2) transition at 345 GHz were made with the ASTE telescope at Pampa la Bola in Chile (Ezawa et al. 2004) in 2004 October. The half-power beam width was measured to be 22″ at 345 GHz by observing the planets. This corresponds to 5.3 pc at the distance of the LMC, 50 kpc. The telescope was equipped with a single "cartridge-type" SIS receiver, sensitive from 324 to 384 GHz, which is of a similar design to that for ALMA (Kohno 2005). The spectrometer was an XF-type digital autocorrelator (Sorai et al. 2000) and was used in the wideband mode, which has a bandwidth of 512 MHz with 1024 channels. The spectrometer provided a velocity coverage and resolution of 450 and 0.44 km s^{-1}, respectively, at 345 GHz. We observed six GMCs (seven regions) in the Large Magellanic Cloud as shown in Figure 1 and listed in Table 1. These observations were carried out by position switching at a grid spacing of 20″ or 30″ for the entire clouds and of 10″ or 15″ for the regions around the local peaks of the integrated intensity. The pointing error was measured to be within 7″ in peak to peak by observing CO point sources R Dor or o Cet every 2 hr during this observing term. The spectral intensities were calibrated by employing the standard room-temperature chopper-wheel technique. We observed Ori-KL once a day, and N159W every 2 hr to check the stability of the intensity calibration, and the intensity variation during these observations was less than 13%. We use 0.7 for the main-beam efficiency at 345 GHz, which was measured by

TABLE 1
LIST OF OBSERVED GMCS AND TRANSITIONS

GMC				Position			Telescope		
No.[a]	Name[a]	Type[b]	Region Name	α(1950)	δ(1950)	Ref.	^{12}CO($J = 3$–2)	^{12}CO($J = 1$–0)	^{13}CO($J = 1$–0)
(1)	(2)	(3)	(4)	(5)	(6)	(7)	(8)	(9)	(10)
186.....	LMC N J0538−6904	III	30 Dor	5 39 0.2	−69 8 0.0	1	ASTE	MOPRA	SEST[c]
197.....	LMC N J0540−7008	III	N159	5 40 18.2	−69 47 0.0	1	ASTE	MOPRA	SEST[c]
			N171	5 40 24.1	−70 8 0.0	2	ASTE	MOPRA	...
216.....	LMC N J0544−6923	II	N166	5 44 52.5	−69 26 39.1	3	ASTE	SEST[d]	SEST[d]
153.....	LMC N J0530−7106	III	N206	5 31 33.9	−71 10 0.0	4	ASTE	SEST	SEST
156.....	LMC N J0532−7114	II	N206D	5 32 52.2	−71 16 0.0	4	ASTE	SEST	SEST
225.....	LMC N J0547−7041	I	GMC 225	5 48 35.7	−70 40 0.0	4	ASTE	SEST	SEST

NOTES.— Units of right ascension are hours, minutes, and seconds, and units of declination are degrees, arcminutes, and arcseconds. Col. (1): Running number of GMC used in Table 1 in Fukui et al. (2007). Col. (2): Name of GMC. Col. (3): Type of GMC. Col. (4): Region name used in this paper. Cols. (5)–(6): Coordinates used as reference position in each region for these ^{12}CO($J = 3$–2) observations. Col. (7): References for the positions. Cols. (8)–(10): Telescope used for each observation.

[a] Fukui et al. (2007).

[b] Kawamura et al. (2007).

[c] Johansson et al. (1998).

[d] Garay et al. (2002).

REFERENCES.— (1) Johansson et al. 1998; (2) Kutner et al. 1997; (3) Garay et al. 2002; (4) Mizuno et al. 2001.

observing Jupiter. The system noise temperature was typically 300 K in double-sideband (DSB) including the atmosphere toward the zenith. The typical rms noise fluctuations were ~0.25 K at a velocity resolution of 0.44 km s^{-1} for a 1 minute integration for an on-position. In total, about 1400 points were observed in equatorial coordinates (B1950). Velocities were relative to the local standard of rest (LSR). These observations were made remotely from an ASTE operations room in San Pedro de Atacama, Chile, using the network observation system N-COSMOS3 developed by NAOJ (Kamazaki et al. 2005).

2.3. ^{12}CO($J = 1$–0) *and* ^{13}CO($J = 1$–0)

2.3.1. *Mopra Observations*

A $20' \times 120'$ region, the prominent molecular ridge extending from 30 Doradus southward, was mapped in the $J = 1$–0 transition of ^{12}CO at a frequency of 115 GHz with the 22 m ATNF Mopra telescope, in five runs from 2005 May to September. This region contains the 30 Dor, N159, and N171 regions. The newly implemented on-the-fly (OTF) mode was used, in which the telescope takes data continuously while moving across the sky. Spectra were taken at a $6''$ spacing so that the $33''$ Mopra beam would be well oversampled in the scanning direction; the row spacing was $8''$, also assuring oversampling. The typical system noise temperature, $T_{\rm sys}$, was 500 K in the single sideband (SSB) toward the zenith. The pointing was checked on the SiO maser R Dor every 2 hr; typical pointing error was less than $5''$ rms. The digital correlator was configured to output 1024 channels across 64 MHz in each of two orthogonal polarizations. The velocity resolution and coverage were 0.16 and 160 km s^{-1}, respectively, at 115 GHz. The observing time was about 100 minutes per field ($5' \times 5'$), providing rms noise fluctuations of ~0.34 K at a velocity resolution of 0.65 km s^{-1}. Initial spectral processing (baseline fitting and calibration onto a T_A^* scale) was performed using the `livedata` task in AIPS++, and the spectra were gridded into data cubes using the AIPS++ `gridzilla` task. During the gridding, a Gaussian smoothing kernel with a FWHM taken at one-half of the beam size was convolved with the data, so the effective resolution of the output cubes was $36''$. The cubes were then rescaled onto a $T_{\rm mb}$ scale using an "extended beam" efficiency of 0.55 (Ladd et al. 2005). This takes into account that sources larger than about $80''$ in diameter will couple to both the main beam and the inner error beam of the telescope. The cubes were two-dimensional Gaussian smoothed to a $45''$ beam, which is the beam size of SEST at 115 GHz.

2.3.2. *SEST Observations*

Observations toward the N206, N206D, and GMC 225 regions in the ^{12}CO($J = 1$–0) line (115 GHz) were made in 2001 August and 2002 February using the SEST 15 m telescope at La Silla, Chile. The HPBW was $45''$ at 115 GHz, the front end was the IRAM 115 SIS receiver, and the spectrometer was a high-resolution AOS with 2048 channels. The typical system noise temperature was 550 K (SSB). The velocity resolution and coverage were 0.2 and 216 km s^{-1}, respectively, at 115 GHz. We mapped these three regions in position switching with a grid spacing of $40''$ or $20''$. The typical integration time was 1 minute for an on-position, providing rms noise fluctuations of ~0.18 K at a velocity resolution of 0.2 km s^{-1}.

Observations toward the N206, N206D, and GMC 225 regions in the ^{13}CO($J = 1$–0) line (110 GHz) were made in 2002 February and December 2002, also using the SEST 15 m telescope. We mapped peak positions of ^{12}CO($J = 1$–0) in position switching with a grid spacing of $20''$. The system noise temperature was typically 230 K (SSB). The typical integration time was 4 minutes for an on-position, providing rms noise fluctuations of ~0.04 K at a velocity resolution of 0.2 km s^{-1}.

The pointing accuracy was $5''$ rms. We checked this by observing the SiO maser toward R Dor every 2 hr during this observing term. N159W was observed periodically for pointing checks and intensity calibration. We use 0.8 for the main-beam efficiency at 115 GHz by assuming the main-beam temperature $T_{\rm mb}$ of N159W to be ~6.5–6.9 K to keep consistency with previous publications (Johansson et al. 1994, 1998).

Observations toward the N166 region were also made using the SEST 15 m telescope. The details are described separately by Garay et al. (2002).

3. RESULTS

We first present the ^{12}CO($J = 3$–2) images of the clouds at 5 pc resolution and compare them empirically with the ^{12}CO($J = 1$–0) distribution (§ 3.1). Next, we define molecular clumps and estimate the physical parameters of each clump (§ 3.2).

3.1. *Distributions of the* ^{12}CO($J = 3$–2) *Emission*

In Figure 2, typical ^{12}CO($J = 3$–2) and ^{12}CO($J = 1$–0) profiles of the 30 Dor, N159, and GMC 225 regions are presented. The upper panels, Figures 2*a*–2*c*, show ^{12}CO($J = 3$–2) profiles. These illustrate the low noise levels of the present data, typically ~0.25 K rms at 0.44 km s^{-1} velocity resolution. Among the present observed positions, the ^{12}CO($J = 3$–2) intensity is strongest at $T_{\rm mb} \sim 12.3$ K toward N159W (Fig. 2*b*). The lower panels, Figures 2*d*–2*f*, show ^{12}CO($J = 1$–0) profiles toward the same positions, where the gray line indicates ^{12}CO($J = 3$–2) profiles convolved to a $45''$ Gaussian beam following the method described in § 4. The ^{12}CO($J = 3$–2) intensities from the 30 Dor and N159 regions are a little stronger than the ^{12}CO($J = 1$–0) intensity when convolved to the same resolution. Only toward GMC 225 is the ^{12}CO($J = 3$–2) intensity about 50% weaker than the ^{12}CO($J = 1$–0) intensity. The peak velocity and line width are nearly the same between the two transitions in these regions.

The distributions of the integrated intensities of ^{12}CO($J = 3$–2) and ^{12}CO($J = 1$–0) are shown in Figures 3–9. Detailed descriptions of each region are presented in the following.

3.1.1. *30 Dor* (*Fig. 3*)

Figures 3*a* and 3*b* show the distributions of the ^{12}CO($J = 3$–2) and ^{12}CO($J = 1$–0) integrated intensities in the 30 Dor region. We see a general trend that the $J = 3$–2 distribution shows more details that are not obvious in the $J = 1$–0 distribution owing to the higher angular resolution and possibly due to the more compact distribution of warmer and denser gas in $J = 3$–2 than in $J = 1$–0. We see three peaks corresponding to the ^{12}CO($J = 1$–0) peaks, 30 Dor-10, 30 Dor-6, and 30 Dor-12, reported in Johansson et al. (1998). One of them in the north, 30 Dor-06, which is singly peaked in $J = 1$–0, appears to be resolved into two peaks with the present beam.

3.1.2. *N159* (*Fig. 4*)

Figures 4*a* and 4*b* show the ^{12}CO($J = 3$–2) and ^{12}CO($J = 1$–0) distributions in N159. We note that N159W shows the strongest intensity among the present clouds, as well as a very compact peak that is not sufficiently resolved with the present beam. Its radius is estimated to be a few parsecs after deconvolution. N159E also shows a compact distribution with a hint of a subpeak, while N159S shows similar distributions in both $J = 1$–0 and $J = 3$–2.

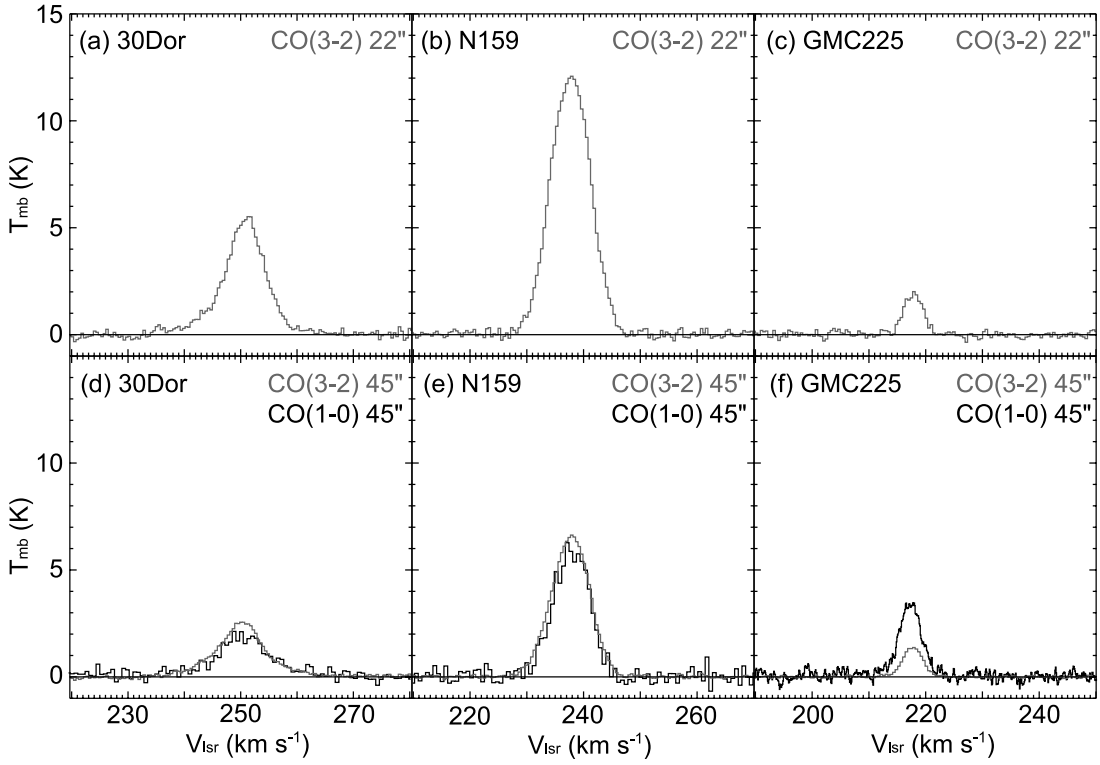

FIG. 2.—^{12}CO($J = 3$–2) and ^{12}CO($J = 1$–0) profiles at selected points. Note that the vertical scale is main-beam temperature, $T_{\rm mb}$. The velocities (abscissae) are relative to the LSR. (*a*) ^{12}CO($J = 3$–2) profile of 30 Dor. (*b*) ^{12}CO($J = 3$–2) profile of N159. (*c*) ^{12}CO($J = 3$–2) profile of GMC 225. (*d*) ^{12}CO($J = 1$–0) and smoothed ^{12}CO($J = 3$–2) profiles of 30 Dor. (*e*) ^{12}CO($J = 1$–0) and smoothed ^{12}CO($J = 3$–2) profiles of N159. (*f*) ^{12}CO($J = 1$–0) and smoothed ^{12}CO($J = 3$–2) profiles of GMC 225. [*See the electronic edition of the Supplement for a color version of this figure.*]

The east-west elongation of N159S may be due to the scanning effect of the OTF mapping and needs to be confirmed.

3.1.3. *N171* (*Fig. 5*)

Figures 5*a* and 5*b* show the ^{12}CO($J = 3$–2) and ^{12}CO($J = 1$–0) distributions in N171. We note that the $J = 3$–2 emission is weaker than the $J = 1$–0 emission. There are multiple velocity components, at $V_{\rm LSR} = 225$, 230, and 240 km s^{-1} in both $J = 3$–2 and $J = 1$–0 as indicated in Table 2 and Table 1 of Kutner et al. (1997).

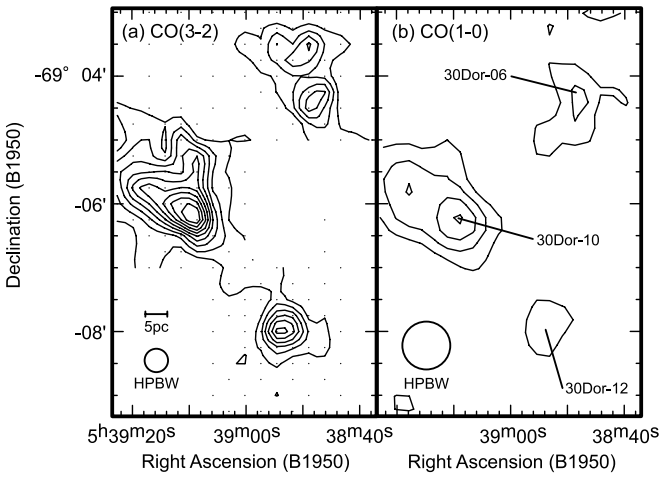

FIG. 3.—(*a*) Contour map of ^{12}CO($J = 3$–2) integrated intensity in the 30 Doradus region. The contour levels are 5, 10, 15, 20, 25, 30, 35, 40, and 45 K km s^{-1}. Observed points are indicated by dots. (*b*) Contour map of ^{12}CO($J = 1$–0) integrated intensity in the 30 Doradus region. The contour levels are 10, 15, 20, and 25 K km s^{-1}.

3.1.4. *N166* (*Fig. 6*)

Figures 6*a* and 6*b* show the ^{12}CO($J = 3$–2) and ^{12}CO($J = 1$–0) distributions in N166. The $J = 1$–0 data themselves have already been published by Garay et al. (2002). We see four peaks in both $J = 3$–2 and $J = 1$–0. Of these peaks, three peaks are named Cloud-B, Cloud-C, and Cloud-D, as reported by Garay et al. (2002), although Cloud-C is resolved into two peaks with the present beam and observing grid.

3.1.5. *N206* (*Fig. 7*)

Figures 7*a* and 7*b* show the ^{12}CO($J = 3$–2) and ^{12}CO($J = 1$–0) distributions in N206. A $J = 1$–0 peak appears to be resolved into two subpeaks and a north-south filamentary structure with the higher angular resolution of the $J = 3$–2 line.

3.1.6. *N206D* (*Fig. 8*)

Figures 8*a* and 8*b* show the ^{12}CO($J = 3$–2) and ^{12}CO($J = 1$–0) distributions in N206D. We can see a head-tail structure in $J = 3$–2, although it appears more rounded in $J = 1$–0.

3.1.7. *GMC 225* (*Fig. 9*)

Figures 9*a* and 9*b* show the ^{12}CO($J = 3$–2) and ^{12}CO($J = 1$–0) distributions in GMC 225. We note that $J = 3$–2 emissions are weaker than those of $J = 1$–0.

3.2. *Properties of the Clumps*

We identified clumps in the following way in the $J = 3$–2 distributions shown in Figures 3–9: (1) Pick up local peaks using the integrated intensity. (2) Draw a contour at one-half the peak

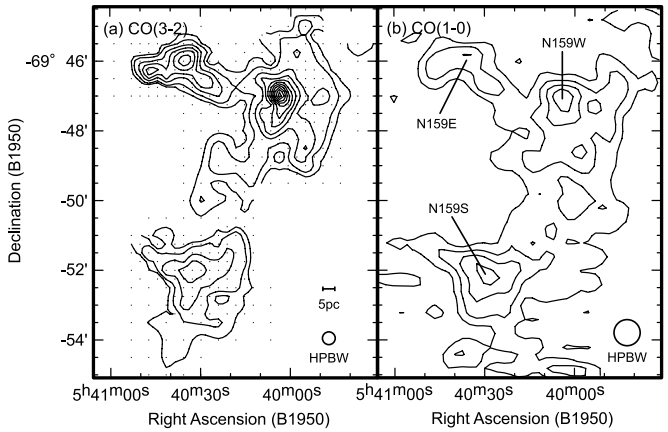

FIG. 4.—(*a*) Contour map of ^{12}CO($J = 3$–2) integrated intensity in the N159 region. The contour levels are 5, 10, 20, 30, 40, 50, 60, 70, 80, 90 and 100 K km s^{-1}. Observed points are indicated by dots. (*b*) Contour map of ^{12}CO($J = 1$–0) integrated intensity in the N159 region. The contour levels are 10, 20, 30, and 40 K km s^{-1}.

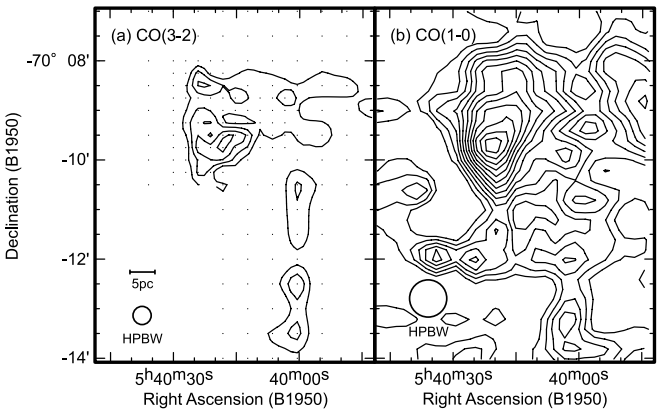

FIG. 5.—(*a*) Contour map of ^{12}CO($J = 3$–2) integrated intensity in the N171 region. The contour levels are 8, 12, 16, and 20 K km s^{-1}. Observed points are indicated by dots. (*b*) Contour map of ^{12}CO($J = 1$–0) integrated intensity in the N171 region. The contour levels are 8, 12, 16, 20, 24, 28, 32, 36, 40, 44, 48, and 52 K km s^{-1}.

integrated intensity level and identify it as a clump unless it contains other local peaks. (3) When there are other local peaks inside the contour, draw new contours at the 70% level of each integrated intensity peak. Then, identify clumps separately if their contours do not contain another local peak (the boundary is taken at the "valley" between clumps), or else identify a clump by using the highest contour as a clump boundary. (4) If a spectrum has multiple velocity components with a separation of more than 6 km s^{-1}, identify these components to be associated with different clumps.

As a result, 32 clumps have been identified: five clumps in the 30 Dor region, 10 clumps in the N159 region, six clumps in the N171 region, five clumps in the N166 region, two clumps in the N206 region, one clump in the N206D region, and three clumps in the GMC 225 region. Their line parameters at the peak positions are shown in Table 2, and their physical properties are listed in Table 3. The clump size, line width, and virial mass lie in the range 1.1–12.4 pc, 4.0–12.8 km s^{-1}, and 4.6×10^3 to 2.2×10^5 $M_\odot$, respectively. The smallest clump identified by the procedure above is detected with two observing points, and its size is 1.1 pc. There are several other weak emissions (below 6 σ), and they are detected with one observing point. These emissions are not identified as clumps. When we assume that such small clumps ($R \sim 1$ pc, $dV \sim 7$ km s^{-1}) exist, their virial mass is 9.3×10^3 $M_\odot$, and this corresponds to the detection limit. There are 18 local peaks above the 6 σ noise level that are not identified as clumps, because the stronger peaks are located near these local peaks. Their virial mass is 6.5×10^4 $M_\odot$ if their size and line width are similar to those of identified clumps ($R \sim 7$ pc, $dV \sim 7$ km s^{-1}). This seems to correspond to the completeness limit.

If the clumps are identified with the 70% level of the peak integrated intensity instead of the 50% level, the clump size changes to one-half the original one, although the line width does not change. Their virial mass also changes to about one-half the original one. Histograms of their physical properties are presented in Figure 10. Typical values are 7 pc, 7 km s^{-1}, and 6×10^4 $M_\odot$, in size, line width, and virial mass, respectively. Their line widths are larger than those of the GMCs in our galaxy (e.g., Williams & Blitz 1998; Ikeda et al. 1999; Sun et al. 2006). We note a trend that the masses of these clumps are relatively large compared with those of high-mass cloud cores in the Milky Way, which are of the order of 10^3 $M_\odot$ (e.g., Burton et al. 2005; Yonekura et al. 2005). Precise comparisons will be necessary using same tracers and resolution in the future because those Galactic studies above are based on optically thin millimeter dust continuum and C^{18}O emission. The clumps in the LMC are also fairly compact, with sizes of several parsecs or less. Hereafter, the region names and the numbers of clumps are used to identify clumps (e.g., "30 Dor No. 1").

4. DATA ANALYSIS

4.1. *Derivation of Line Intensity Ratios*

The spatial resolution of the present CO data varies depending on the telescope and frequency. We convolved and regridded these data into the same resolution and position using two-dimensional Gaussian smoothing in order to compare them to derive reliable peak intensity ratios of ^{12}CO($J = 3$–2) to ^{12}CO($J = 1$–0) (hereafter, $R_{3-2/1-0}$).

We made Gaussian fits to each of the ^{12}CO($J = 3$–2) and ^{12}CO($J = 1$–0) spectra having a single peak in most cases. We derived peak intensities and FWHM line widths through these fittings. The ratios of the two transitions were then derived as the ratio between peak values of $T_{\rm mb}$. The distributions of these ratios are shown along with the ^{12}CO($J = 1$–0) distributions in panels (*a*) of Figures 11–17. The youngest stellar clusters SWB0, whose ages are estimated to be less than 10 Myr, are also shown by gray or black circles (Bica et al. 1996).

The averaged $R_{3-2/1-0}$ over each clump (hereafter, $R_{3-2/1-0,\rm clump}$) was also derived from the averaged ^{12}CO($J = 3$–2) and ^{12}CO($J = 1$–0) spectra over each clump. A summary of the $R_{3-2/1-0,\rm clump}$ for each clump is shown in Table 4. The histogram in Figure 18 shows that the $R_{3-2/1-0,\rm clump}$ ranges from 0.2 to 1.6. These ratios will be compared with numerical calculations of radiative transfer in the LVG approximation to derive constraints on density and temperature.

4.2. *LVG Analysis*

4.2.1. *Calculations of LVG Model*

To estimate the physical properties of the molecular gas in the LMC, we performed an LVG analysis (Goldreich & Kwan 1974) of the CO rotational transitions. The LVG radiative transfer code simulates a spherically symmetric cloud of constant density and temperature with a spherically symmetric velocity distribution proportional to the radius and employs a Castor escape probability formalism (Castor 1970). It solves the equations of statistical equilibrium for the fractional population of CO rotational levels

TABLE 2

OBSERVED PROPERTIES OF ^{12}CO($J = 3$–2) CLUMPS

		Position		Peak Properties				
Region	No.	α(1950)	δ(1950)	T_{mb} (K)	V_{LSR} (km s^{-1})	ΔV (km s^{-1})	Integrated Intensity (K km s^{-1})	Other ID
(1)	(2)	(3)	(4)	(5)	(6)	(7)	(8)	(9)
30 Dor	1	5 39 8.6	−69 6 15	5.2	250.4	8.4	49.5	30Dor-10[a]
	2	5 38 54.6	−69 8 0	4.3	246.9	6.9	31.7	30Dor-12[a]
	3	5 38 49.0	−69 4 30	3.1	251.9	5.4	22.5	
	4	5 38 49.0	−69 3 30	2.6	248.2	5.0	21.1	30Dor-06[a]
	5	5 38 54.6	−69 9 0	1.2	247.4	4.5	5.3	
N159	1	5 40 3.7	−69 47 0	12.3	237.3	8.1	106.6	N159-W[a]
	2	5 40 35.5	−69 46 0	7.6	233.2	7.0	55.5	N159-E[a]
	3	5 40 47.1	−69 46 15	5.4	234.6	6.7	46.0	
	4	5 40 32.7	−69 52 0	3.5	234.4	9.7	35.4	N159-S[a]
	5	5 39 49.3	−69 47 0	3.0	233.5	9.5	29.7	
	6	5 40 47.2	−69 51 30	3.6	235.6	5.3	19.8	
	7	5 39 55.1	−69 45 0	4.5	238.3	3.4	16.6	
	8	5 40 29.8	−69 50 0	0.91	234.6	6.9	10.5	
	9	5 40 41.4	−69 51 0	0.87	235.7	8.0	9.3	
	10	5 39 37.7	−69 45 30	0.89	238.6	7.9	8.3	
N171	1	5 40 0.5	−70 12 30	2.5	224.3	5.2	15.4	30DOR-CENTER-04[b]
	2	5 40 0.5	−70 10 30	1.3	227.3	8.3	12.7	
	3	5 40 24.1	−70 9 45	1.3	230.9	9.2	18.2	
	4	5 40 24.1	−70 8 30	2.3	231.0	6.7	16.1	30DOR-CENTER-03[b]
	5	5 40 6.4	−70 9 0	1.7	240.6	4.9	11.5	
	6	5 40 18.2	−70 9 30	1.9	240.7	5.1	10.4	
N166	1	5 44 58.2	−69 26 39	4.5	227.6	4.5	22.1	Cloud-C[c]
	2	5 44 46.8	−69 27 24	2.9	229.4	6.2	20.3	
	3	5 45 3.9	−69 29 9	2.2	227.9	5.5	14.6	Cloud-D[c]
	4	5 44 32.6	−69 23 39	1.0	236.1	9.2	10.1	Cloud-B[c]
	5	5 45 9.6	−69 30 9	0.82	231.6	4.5	9.6	
N206	1	5 31 29.8	−71 9 40	5.1	229.0	4.6	26.2	
	2	5 31 46.3	−71 8 20	2.3	231.2	4.6	13.5	
N206D	1	5 32 58.4	−71 15 20	4.5	224.6	4.0	18.9	
GMC 225	1	5 47 51.3	−70 41 20	1.8	216.5	3.9	9.0	
	2	5 48 25.6	−70 41 20	1.2	216.2	6.2	8.6	
	3	5 48 53.9	−70 40 30	1.8	216.4	3.8	7.9	

NOTES.— Units of right ascension are hours, minutes, and seconds, and units of declination are degrees, arcminutes, and arcseconds. Col. (1): Region. Col. (2): Running number in each region. Cols. (3)–(4): Positions of observed points with maximum ^{12}CO($J = 3$–2) integrated intensities within the ^{12}CO($J = 3$–2) clumps given in equatorial coordinates. Cols. (5)–(8): Observed properties of the ^{12}CO($J = 3$–2) spectra obtained at the peak positions of the ^{12}CO($J = 3$–2) clumps. The peak main-beam temperature T_{mb}, V_{LSR}, and the FWHM line width ΔV are derived from a single Gaussian fitting and are given in cols. (5), (6), and (7), respectively. In col. (8), the ^{12}CO($J = 3$–2) integrated intensities at the peak positions of the ^{12}CO($J = 3$–2) clumps are shown. Col. (9): Another identification based on ^{12}CO($J = 1$–0) observations with SEST.

[a] Johansson et al. (1998).

[b] Kutner et al. (1997).

[c] Garay et al. (2002).

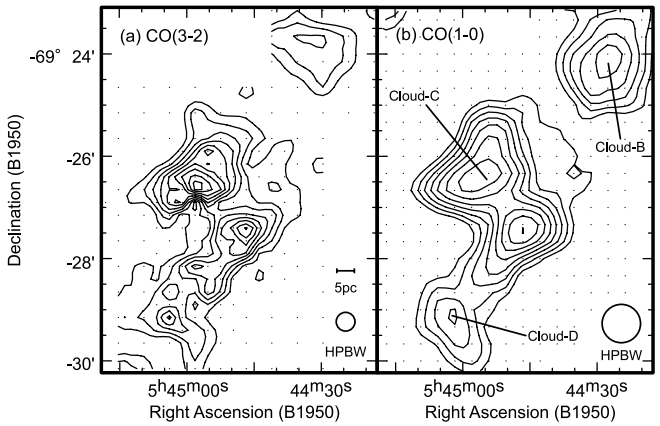

FIG. 6.—(*a*) Contour map of ^{12}CO($J = 3$–2) integrated intensity in the N166 region. The contour levels are 6, 8, 10, 12, 14, 16, 18, 20, and 22 K km s^{-1}. Observed points are indicated by dots. (*b*) Contour map of ^{12}CO($J = 1$–0) integrated intensity in the N166 region. The contour levels are 8, 10, 12, 14, 16, 18, 20, and 22 K km s^{-1}. Observed points are indicated by dots.

at each density and temperature. It includes the lowest 40 rotational levels of the ground vibrational level and uses the Einstein A and H_2 impact rate coefficients of Schöier et al. (2005).

The present calculations incorporate the lowest 40 rotational levels of CO in the ground vibrational state over a kinetic temperature range of $T_{\rm kin} = 5$–200 K and a density range of $n(\rm H_2) = 10$–10^6 cm^{-3}. We did not include higher energy levels in the present study, which requires including populations in the lower vibrationally excited states. Therefore, the present work does not cover kinetic temperatures above 200 K, which should be dealt with in the future for analyses of higher submillimeter transitions above $J = 4$–3. This imposes a limit of $T_{\rm kin} \sim 200$ K in the present study, and even higher temperature is not excluded in general below.

We performed calculations for three different CO fractional abundances: $X(\rm CO) = [CO]/[H_2] = 1 \times 10^{-6}$, 3×10^{-6}, and 1×10^{-5}, and three different ^{12}CO/^{13}CO abundance ratios of 20, 25, and 30 (Heikkilä et al. 1999).

4.2.2. *Results from* ^{12}CO($J = 3$–2) *and* ^{12}CO($J = 1$–0) *Data for 32 Clumps*

First, we assume that X(CO) is uniform among the clumps and derive density and temperature using the LVG results. Figure 19*a*

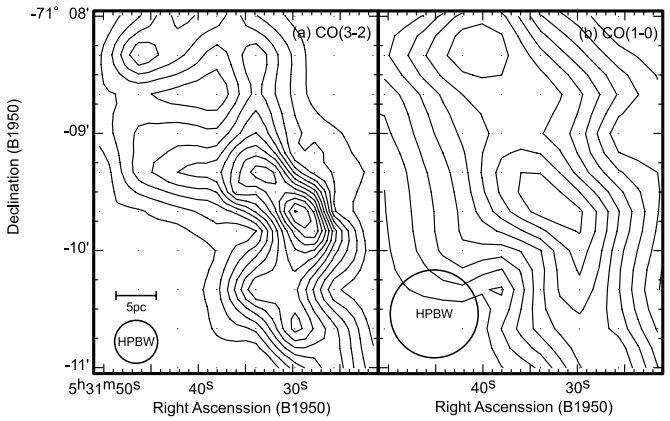

FIG. 7.—(*a*) Contour map of ^{12}CO($J = 3$–2) integrated intensity in the N206 region. The contour levels are 4, 6, 8, 10, 12, 14, 16, 18, 20, 22, 24, and 26 K km s^{-1}. Observed points are indicated by dots. (*b*) Contour map of ^{12}CO($J = 1$–0) integrated intensity in the N206 region. The contour levels are 4, 6, 8, 12, 14, 16, and 18 K km s^{-1}. Observed points are indicated by dots.

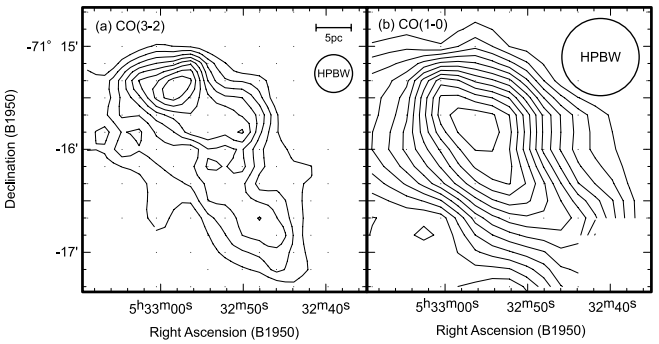

FIG. 8.—(*a*) Contour map of ^{12}CO($J = 3$–2) integrated intensity in the N206D region. The contour levels are 4, 6, 8, 10, 12, 14, 16, and 18 K km s^{-1}. Observed points are indicated by dots. (*b*) Contour map of ^{12}CO($J = 1$–0) integrated intensity in the N206D region. The contour levels are 4, 6, 8, 10, 12, 14, 16, 18, 20, 22, 24, and 26 K km s^{-1}. Observed points are indicated by dots.

illustrates that we obtain the following lower limits for kinetic temperature and density. For the eight clumps with $R_{3-2/1-0,\rm clump} \geq 1$ (30 Dor Nos. 1, 2, 3, 4, N159 Nos. 1, 2, 6, 8), we estimate $T_{\rm kin} > 30$ K and $n(\rm H_2) > 10^3$ cm^{-3}. For the 24 clumps with $R_{3-2/1-0,\rm clump} < 1$ (30 Dor No. 5, N159 Nos. 3, 4, 5, 7, 9, 10, N171 Nos. 1, 2, 3, 4, 5, 6, N166 Nos. 1, 2, 3, 4, 5, N206 Nos. 1, 2, N206D No. 1, GMC 225 Nos. 1, 2, 3), we estimate $T_{\rm kin}$ greater than several kelvins and $n(\rm H_2)$ greater than several times 10^2 cm^{-3}. In either case, the lower limits tend to increase with $R_{3-2/1-0,\rm clump}$.

4.2.3. *Results from* ^{12}CO($J = 3$–2), ^{12}CO($J = 1$–0), *and* ^{13}CO($J = 1$–0) *Data for 13 Clumps*

We can better constrain these physical parameters when ^{13}CO($J = 1$–0) data are available. Figure 19 shows the general behavior of the loci of constant $R_{3-2/1-0}$ and constant $R_{12/13}$ [peak intensity ratio of ^{12}CO($J = 1$–0) to ^{13}CO($J = 1$–0)] in the density-temperature plane. It is recognized that the combination of the two will allow us to determine the parameters relatively well, since the two lines are nearly "orthogonal" in the plane, except for densities higher than $\sim 10^4$ cm^{-3} (Fig. 19).

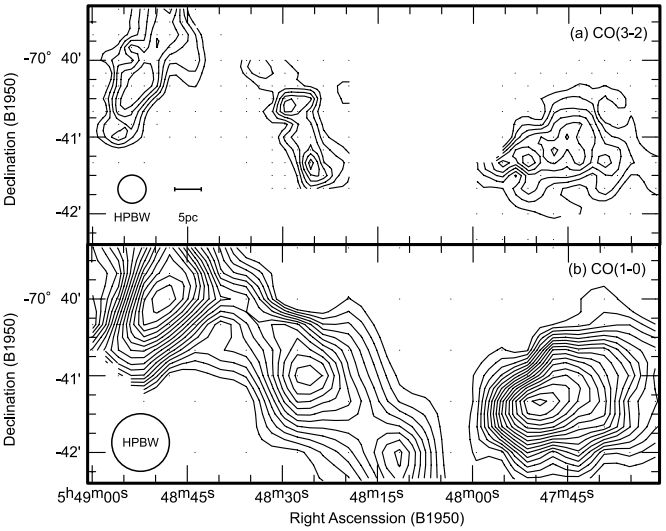

FIG. 9.—(*a*) Contour map of ^{12}CO($J = 3$–2) integrated intensity in the GMC 225 region. The contour levels are 3, 4, 5, 6, 7, and 8 K km s^{-1}. Observed points are indicated by dots. (*b*) Contour map of ^{12}CO($J = 1$–0) integrated intensity in the GMC 225 region. The contour levels are 3, 4, 5, 6, 7, 8, 9, 10, 11, 12, 13, 14, 15, 16, 17, 18, and 19 K km s^{-1}. Observed points are indicated by dots.

TABLE 3

PHYSICAL PROPERTIES OF ^{12}CO($J = 3$–2) CLUMPS

		CLUMP PROPERTIES		
REGION	NO.	$\Delta V_{\rm clump}$ (km s^{-1})	$R_{\rm deconv}$ (pc)	$M_{\rm vir}$ ($\times 10^4\ M_\odot$)
(1)	(2)	(3)	(4)	(5)
30 Dor.....	1	12.8	7.2	22
	2	6.9	3.1	2.9
	3	5.8	3.1	2.0
	4	4.0	3.7	1.1
	5	4.6	1.1	0.46
N159.....	1	8.7	4.7	6.8
	2	7.3	6.9	6.9
	3	7.6	4.7	5.2
	4	8.5	11.3	15
	5	10.2	4.7	9.4
	6	5.2	4.3	2.2
	7	4.1	2.3	0.73
	8	6.3	6.3	4.7
	9	7.1	2.3	2.2
	10	7.7	2.3	2.7
N171.....	1	6.5	6.6	5.2
	2	6.9	8.3	7.4
	3	7.2	7.8	7.7
	4	6.2	5.9	4.3
	5	6.1	7.5	5.3
	6	5.6	5.9	3.5
N166.....	1	6.1	9.9	6.9
	2	6.5	9.5	7.6
	3	6.3	10.3	7.7
	4	9.2	12.4	20
	5	9.5	4.7	8.1
N206.....	1	6.6	7.1	5.9
	2	5.2	6.3	3.2
N206D.....	1	4.0	7.3	2.2
GMC 225.....	1	4.2	8.8	3.1
	2	6.6	5.5	4.6
	3	4.9	8.8	3.9

NOTES.—Col. (1): Region. Col. (2): Running number in each region. Col. (3): Line width, $\Delta V_{\rm clump}$, derived by using a single Gaussian fitting for a spectrum obtained by averaging all the spectra within a single clump. Col. (4): Deconvolved effective radii, $R_{\rm deconv}$, defined as $[R^2_{\rm nodeconv} - (\theta_{\rm HPBW}/2)^2]^{0.5}$. The $R_{\rm nodeconv}$ is effective radii defined as $(A/\pi)^{0.5}$, where A is the total cloud surface area. Col. (5): Virial masses of the ^{12}CO($J = 3$–2) clumps; a density profile of $\rho \propto r^{-1}$ was assumed; the virial mass is written as $M_{\rm vir}/M_\odot = 190[\Delta V_{\rm clump}({\rm km\ s^{-1}})]^2 R_{\rm deconv}({\rm pc})$ (MacLaren et al. 1988).

Of the 32 clumps, ^{13}CO($J = 1$–0) data are available for 13 clumps, including four clumps with $R_{3-2/1-0,{\rm clump}} \geq 1$ (30 Dor Nos. 1, 4, N159 Nos. 1, 2) and nine clumps with $R_{3-2/1-0,{\rm clump}} < 1$ (N159 No. 4, N166 Nos. 1, 3, 4, N206 Nos. 1, 2, N206D No. 1, GMC 225 Nos. 1, 3). For these 13 clumps, we made a detailed analysis using the $R_{12/13}$ at peaks of ^{12}CO($J = 1$–0) and have obtained the best constraints.

We summarize the input parameters for the 13 clumps in columns (3)–(5) of Table 5. All the data refer to the ^{12}CO($J = 1$–0) beam size, 45″; the higher transition data have been Gaussian smoothed as described in § 4.1. Clump-averaged dv/dr were used for the calculations. The $R_{3-2/1-0,{\rm clump}}$ and $R_{12/13}$ at the peak of ^{12}CO($J = 1$–0) were used, and the errors of these ratios are both estimated as ±20%, which are derived from errors of absolute intensity calibration. These correspond to 27 σ and 7 σ noise levels of ^{12}CO($J = 3$–2) and ^{12}CO($J = 1$–0), respectively. This indicates that the errors of the intensity ratios are dominated by the error of the absolute intensity calibration. The way clumps are

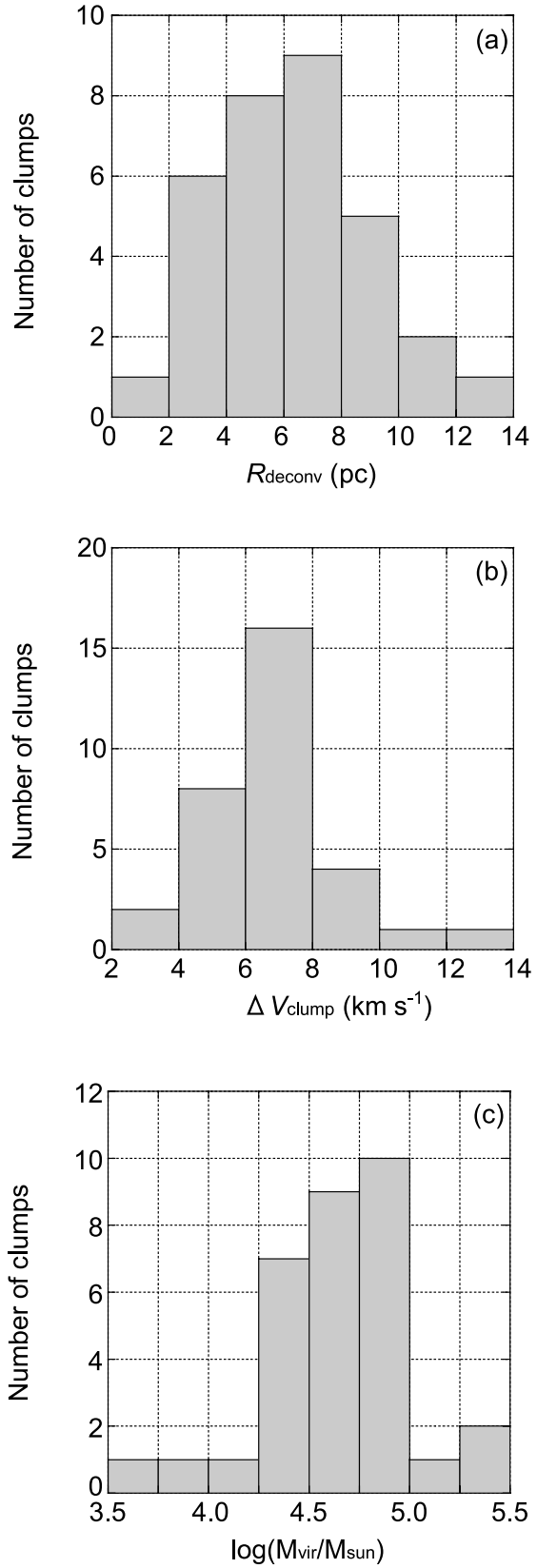

FIG. 10.—Histograms of physical properties of ^{12}CO($J = 3$–2) clumps: (*a*) size, (*b*) line width, and (*c*) virial mass.

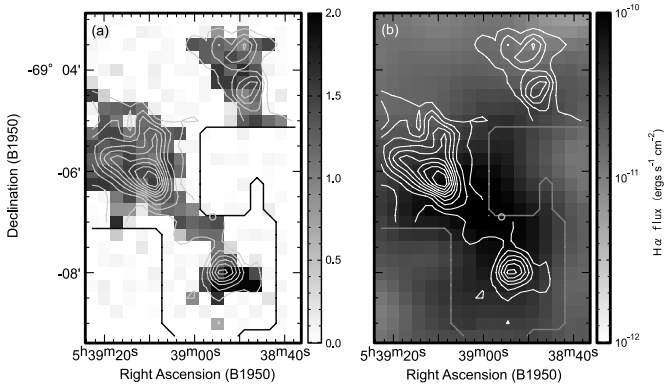

FIG. 11.—(*a*) Color map of $R_{3-2/1-0}$, and (*b*) Hα flux image of the 30 Doradus region. Contours are ^{12}CO($J = 3$–2) integrated intensity. Contour levels are the same as in Fig. 3*a*. Thick lines indicate observed area in ^{12}CO($J = 3$–2); gray circle indicates position of young cluster (<10 Myr; SWB0). [*See the electronic edition of the Supplement for a color version of this figure.*]

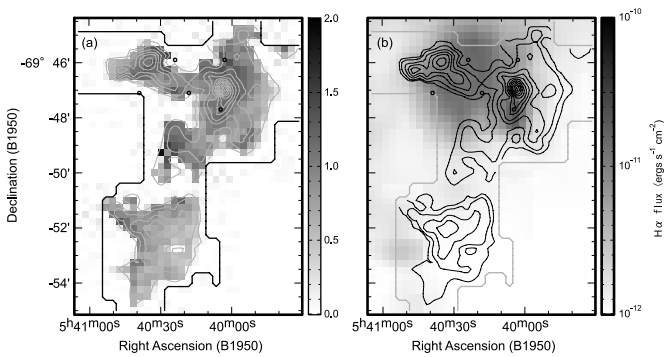

FIG. 12.—(*a*) Color map of $R_{3-2/1-0}$, and (*b*) Hα flux image of the N159 region. Contours are ^{12}CO($J = 3$–2) integrated intensity. Contour levels are the same as in Fig. 4*a*. Thick lines indicate observed area of ^{12}CO($J = 3$–2); black circles indicate positions of young clusters (<10 Myr; SWB0). [*See the electronic edition of the Supplement for a color version of this figure.*]

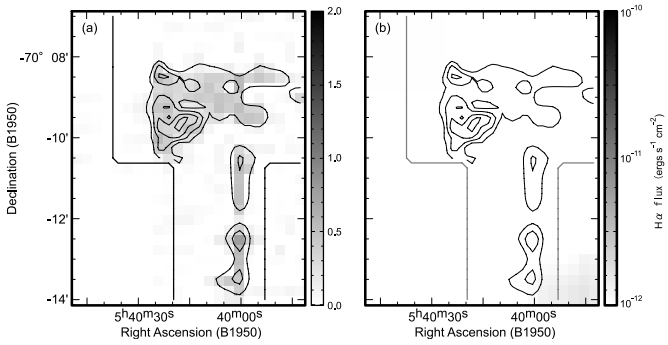

FIG. 13.—(*a*) Color map of $R_{3-2/1-0}$, and (*b*) Hα flux image of the N171 region. Contours are ^{12}CO($J = 3$–2) integrated intensity. Contour levels are the same as in Fig. 5*a*. Thick lines indicate observed area of ^{12}CO($J = 3$–2). [*See the electronic edition of the Supplement for a color version of this figure.*]

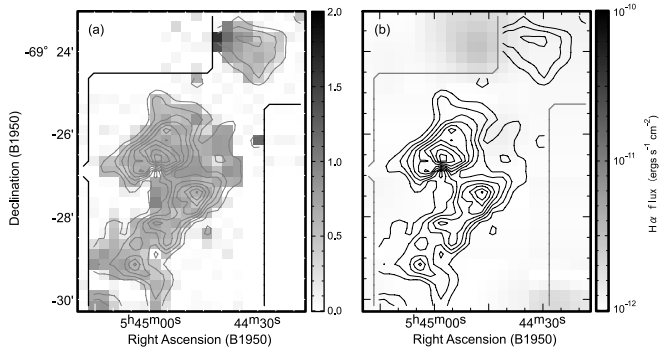

FIG. 14.—(*a*) Color map of $R_{3-2/1-0}$, and (*b*) Hα flux image of the N166 region. Contours are ^{12}CO($J = 3$–2) integrated intensity. Contour levels are the same as in Fig. 6*a*. Thick lines indicate observed area of ^{12}CO($J = 3$–2). [*See the electronic edition of the Supplement for a color version of this figure.*]

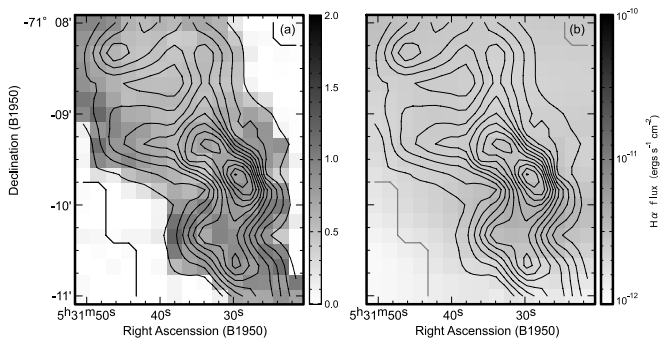

FIG. 15.—(*a*) Color map of $R_{3-2/1-0}$, and (*b*) Hα flux image of the N206 region. Contours are ^{12}CO($J = 3$–2) integrated intensity. Contour levels are the same as in Fig. 7*a*. Thick lines indicate observed area of ^{12}CO($J = 3$–2). [*See the electronic edition of the Supplement for a color version of this figure.*]

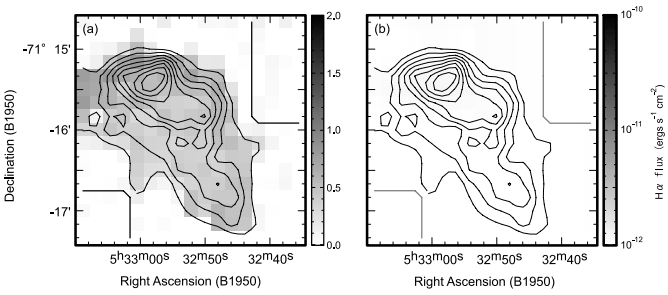

FIG. 16.—(*a*) Color map of $R_{3-2/1-0}$, and (*b*) Hα flux image of the N206D region. Contours are ^{12}CO($J = 3$–2) integrated intensity. Contour levels are the same as in Fig. 8*a*. Thick lines indicate observed area of ^{12}CO($J = 3$–2). [*See the electronic edition of the Supplement for a color version of this figure.*]

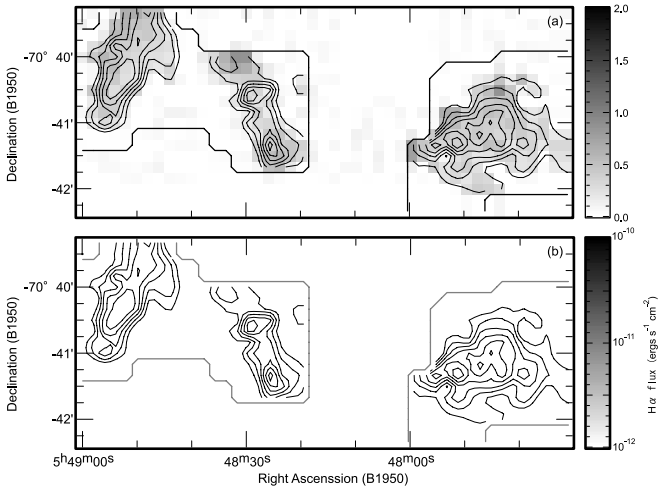

FIG. 17.—(*a*) Color map of $R_{3-2/1-0}$, and (*b*) Hα flux image of the GMC 225 region. Contours are ^{12}CO($J = 3$–2) integrated intensity. Contour levels are the same as in Fig. 9*a*. Thick lines indicate observed area of ^{12}CO($J = 3$–2). [*See the electronic edition of the Supplement for a color version of this figure.*]

defined does not change $R_{3-2/1-0,\mathrm{clump}}$ but changes dv/dr, and dv/dr is about 2 times as large as the original one, when the clumps are identified with the 70% level of the peak integrated intensity level. This, however, does not affect the results of the LVG calculations.

We describe three typical cases: (*a*) 30 Dor No. 1, (*b*) N206 No. 1, and (*c*) GMC 225 No. 1 are shown in Figure 20. A fractional CO abundance of X(CO) of 3×10^{-6} was used throughout. The horizontal axis is molecular hydrogen density [$n(\mathrm{H_2})$], and the vertical axis is the gas kinetic temperature (T_{kin}). Solid lines represent $R_{3-2/1-0,\mathrm{clump}}$, and dashed lines represent $R_{12/13}$ at ^{12}CO($J =$ 1–0) peaks. Hatched areas indicate the overlap regions of these two ratios within the errors, which is allowed from the observed ratios. It also includes the uncertainty due to a possible variation of the ^{12}CO/^{13}CO abundance ratio from 20 to 30. Hereafter, we call clumps above 30 K "warm" and those below "cold." Clumps with densities greater than $10^{3.5}$ cm^{-3} are referred to as "dense" and those at lower densities as "less dense."

30 Dor No. 1 exhibits a $R_{3-2/1-0,\mathrm{clump}}$ of $\sim$1.4, suggesting that it is a warm ($T_{\mathrm{kin}} = 50$–200 K) and dense ($n = 10^3$–10^5 cm^{-3}) clump (Fig. 20*a*). N206 No. 1 (Fig. 20*b*) and GMC 225 No. 1 (Fig. 20*c*) show $R_{3-2/1-0,\mathrm{clump}} \sim 0.7$ and $\sim$0.4, respectively. Figures 20*b* and 20*c* indicate that they are warm ($T_{\mathrm{kin}} = 30$–200 K) and less dense clumps ($n = 10^3$ cm^{-3}) and cold ($T_{\mathrm{kin}} = 15$–40 K) and less dense ($n = 10^3$ cm^{-3}) clumps, respectively. We find that $R_{12/13}$ is useful to discriminate the temperature difference except in the case of 30 Dor No. 1.

All the figures for the 13 clumps for all different fractional CO abundances (1×10^{-6}, 3×10^{-6}, and 1×10^{-5}) are given in Appendix A. In Table 5 we present the results for the 13 clumps for a fixed fractional CO abundance of $X(\mathrm{CO}) = 3 \times 10^{-6}$. The results of previous studies are also summarized in Table 5 for comparison. We find that the present results are the most extensive among these studies in terms of the number of samples, while they are basically consistent with previous studies for the individual clumps or clouds. There are relatively large differences in both density and temperature in N159 No. 4 (N159S) only, and this is because of the high-density tracers used in Heikkilä et al. (1999).

Figure 21 summarizes the calculated densities and temperatures for the 13 clumps. We see first that the temperature ranges from 10 K up to more than 200 K and density from 10^3 to 10^5 cm^{-3}. Clumps that we detected are distributed continuously from cool ($\sim$10–30 K) to warm ($\sim$higher than 30–200 K), and warm clumps are distributed from less dense ($\sim 10^3$ cm^{-3}) to dense ($\sim 10^{3.5}$–10^5 cm^{-3}), although cool clumps are all less dense. The three cases shown in Figure 20 represent typical cases, "warm and dense" [$T_{\mathrm{kin}} \gtrsim 30$–200 K, $n(\mathrm{H_2}) \sim 10^{3.5}$–$10^5$ cm^{-3}], "warm and less dense" [$T_{\mathrm{kin}} \gtrsim 30$–200 K, $n(\mathrm{H_2}) \sim 10^3$ cm^{-3}], and "cool and less dense" [$T_{\mathrm{kin}} \sim 10$–30 K, $n(\mathrm{H_2}) \sim 10^3$ cm^{-3}].

4.2.4. *Effects of X*(CO)

We now discuss the possible effect of changing X(CO), as summarized in Table 6. If we adopt $X(\mathrm{CO}) = 1 \times 10^{-6}$, the contours of $R_{3-2/1-0}$ shift to lower temperature and the contours of $R_{12/13}$ shift to higher density. Accordingly, the solution shifts to lower temperature, higher density. If we adopt $X(\mathrm{CO}) = 1 \times 10^{-5}$, the $R_{3-2/1-0}$ contours shift to higher temperature and the $R_{12/13}$ contours shift to lower density. Accordingly, the solution shifts to higher temperature, lower density (Table 6).

Next, we vary X(CO) from clump to clump. Heikkilä et al. (1999) estimate X(CO) in 30 Dor No. 1 (30 Dor-10), N159 No. 1 (N159W), and N159 No. 4 (N159S) to be 1×10^{-6}, 1×10^{-5}, and 3×10^{-6}, respectively. Table 6 indicates that 30 Dor No. 1 shows similar values to Heikkilä et al. (1999) whereas N159 No. 1 and No. 4 become warmer and lower in density than in Heikkilä et al. (1999). This discrepancy may be due to the fact that the high-density tracers used by Heikkilä et al. (1999) are not used in the present study. To summarize, the assumption of uniform fractional abundance, X(CO), is fairly good and the present results do not show significant difference even if we adopt the different fractional abundances used by previous authors.

4.3. *Comparisons to* Hα *Flux*

4.3.1. *Relation between* $R_{3-2/1-0}$ *and* Hα *Flux*

We converted the Hα data (Kim et al. 1999) toward the present clouds using the method given in Appendix B. The typical background level of the Hα flux is $\sim 10^{-12}$ ergs s^{-1} cm^{-2} at the 40″ scale and ranges up to 10^{-10} ergs s^{-1} cm^{-2} toward strong H II regions (Fig. 22). These data were regridded into the ^{12}CO($J =$ 3–2) data grids. Hα flux images with the youngest stellar clusters SWB0 (Bica et al. 1996; younger than 10 Myr) are shown in panels (*b*) of Figures 11–17, and the ^{12}CO($J = 3$–2) contours from Figures 3–9 are overlaid for comparison in these figures.

Figures 11–17 indicate a clear trend that the $R_{3-2/1-0}$ is enhanced to 1.0–1.5 toward H II regions or clouds with young clusters, as in the 30 Dor and N159 regions. On the other hand, the ratio is low, less than 1.0, toward clumps with neither H II regions nor clusters, as in GMC 225. We also note that the ratio is enhanced toward the regions where Hα is intense or toward the interfaces between clouds and H II regions. A summary of the averaged Hα flux over each clump is shown in Table 4. It is not fully guaranteed that the Hα emission is actually in contact with the molecular gas, and some of the apparent coincidence could be fortuitous. Nonetheless, previous studies comparing CO and Hα flux indicate a strong correlation between them and lend support to the assumption that almost all the coincidences indicate an actual physical association (Fukui et al. 1999; Yamaguchi et al. 2001; A. Kawamura et al. 2008, in preparation).

Figure 23 shows the correlation between $R_{3-2/1-0,\mathrm{clump}}$ and the averaged Hα flux over each clump. It is clear that $R_{3-2/1-0,\mathrm{clump}}$ is well correlated with the averaged Hα flux, with a correlation coefficient of $\sim$0.79. This is a fairly good empirical relationship and should be tested to see if it holds true in other galaxies. The

TABLE 4

^{12}CO($J = 3$–2)/^{12}CO($J = 1$–0) Ratio and Hα Flux

Region (1)	No. (2)	T_{mb}(3–2) (K) (3)	T_{mb}(1–0) (K) (4)	$R_{3-2/1-0,clump}$ (5)	Averaged Hα Flux ($\times 10^{-12}$ ergs s^{-1} cm^{-2}) (6)
30 Dor	1	1.63	1.20	1.4	56.49
	2	1.76	1.12	1.6	73.37
	3	1.56	1.13	1.2	24.09
	4	1.98	1.58	1.3	12.83
	5	0.73	0.87	0.8	39.71
N159	1	5.50	5.04	1.1	9.28
	2	3.69	3.34	1.1	9.37
	3	2.92	3.25	0.9	6.36
	4	2.33	3.34	0.7	1.14
	5	1.84	2.19	0.8	1.93
	6	1.61	1.57	1.0	1.42
	7	1.67	1.98	0.9	3.14
	8	0.78	0.57	1.4	1.52
	9	0.80	0.99	0.8	1.26
	10	0.57	0.84	0.7	1.42
N171	1	1.04	2.20	0.5	1.00
	2	0.69	1.55	0.4	0.93
	3	1.02	3.09	0.3	0.97
	4	1.34	3.89	0.3	0.98
	5	0.88	1.92	0.4	0.95
	6	0.87	2.72	0.3	0.97
N166	1	1.97	3.09	0.6	1.05
	2	1.59	2.60	0.6	1.01
	3	1.17	1.92	0.6	1.06
	4	0.79	1.26	0.6	1.31
	5	0.62	0.92	0.7	1.06
N206	1	1.83	2.39	0.8	3.26
	2	1.34	2.44	0.5	2.68
N206D	1	2.26	4.70	0.5	1.11
GMC 225	1	1.04	2.81	0.4	0.93
	2	0.55	1.62	0.3	0.91
	3	0.77	2.09	0.4	0.92

Notes.—Col. (1): Region. Col. (2): Running number in each region. Col. (3): The peak main-beam temperature, T_{mb}, of the ^{12}CO($J = 3$–2) spectra derived by using a single Gaussian fitting for a spectrum obtained by averaging all the spectra to the beam within a single clump. The intensities refer to the ^{12}CO($J = 1$–0) beam size (45″). Col. (4): Peak main-beam temperature, T_{mb}, of the ^{12}CO($J = 1$–0) spectra derived by using a single Gaussian fitting for a spectrum obtained by averaging all the spectra within a single clump. Col. (5): Ratios of T_{mb}(3–2) to T_{mb}(1–0). Col. (6): Hα flux obtained by averaging within a single clump.

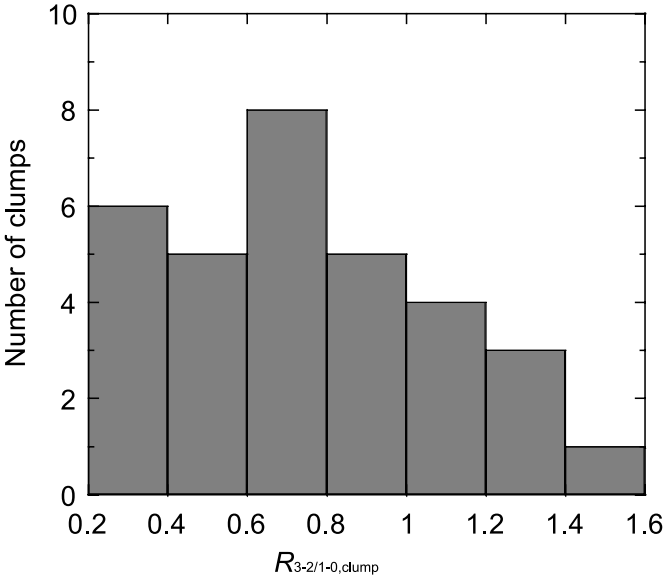

FIG. 18.—Histogram of clump-averaged peak intensity ratio of ^{12}CO($J = 3$–2) to ^{12}CO($J = 1$–0) ($R_{3-2/1-0,\mathrm{clump}}$).

relation suggests that higher $R_{3-2/1-0}$ reflect higher temperatures or higher densities. It is notable that the clumps with averaged Hα flux greater than 10^{-11} ergs s^{-1} cm^{-2} correspond to high $R_{3-2/1-0,\mathrm{clump}}$ of 1.0–1.5. In the barred spiral galaxy M83, the CO($J = 3$–2)/($J = 1$–0) integrated intensity ratio exceeds unity at the nucleus, whereas the ratio gradually decreases to 0.6–0.7 with distance from the center. The ratio is constant through the disk region (Muraoka et al. 2007).

4.3.2. *Comparison with Physical Properties and* Hα *Emission*

Figure 24 shows plots of density and temperature as functions of averaged Hα flux and gives us another insight into these properties. Where averaged Hα is strong (10^{-11} ergs s^{-1} cm^{-2}) the clumps are always warm, at around $T_{\mathrm{kin}} = 100$ K or more. On the other hand, when averaged Hα is weak, density is always low but temperature can be either high or low.

The high-density clumps show high $R_{3-2/1-0,\mathrm{clump}}$ of 1.0–1.5 and are associated with strong Hα flux, while the low-density clumps show low $R_{3-2/1-0,\mathrm{clump}}$ of 0.5–1.0 with weak Hα flux.

Since we are averaging the Hα intensity in each clump, we may be diluting the localized low Hα flux toward some of the clumps in type III and II GMCs. The effects of Hα emission or nearby clusters on the molecular gas are perhaps local phenomena as indicated by the comparison in Figures 11–17 for the individual clumps.

5. DISCUSSIONS

5.1. *Dense and Compact Clumps as Candidates for Protocluster Condensations*

We have carried out submillimeter ^{12}CO($J = 3$–2) observations of GMCs in the LMC that are most extensive and highly sensitive compared to the previous studies. Six GMCs were selected based on the NANTEN CO survey of the LMC, including three type III GMCs actively forming O stars, in addition to three type I/II GMCs that are quiet in O star formation or cluster formation, although the formation of low- to intermediate-mass stars is not excluded. The spatial resolution of ~5 pc and the high sensitivity allowed us to identify 32 molecular clumps in these GMCs and to reveal significant details of the warm and dense molecular gas with $n(\mathrm{H_2}) \sim 10^3$–$10^5$ cm^{-3} and $T_{\mathrm{kin}} \sim 10$–200 K.

The typical mass of the molecular clumps is large, in the range of 5×10^3 to 2×10^5 $M_\odot$ with radii of 1–12 pc. Of all of our objects, N159 No. 1 or W shows the strongest concentration of mass of $\sim 7 \times 10^4$ $M_\odot$ within a radius of ~5 pc. The masses seem to be larger than those of typical Milky Way GMCs such as those in the η Car region (e.g., Yonekura et al. 2005), although the properties of these Galactic GMCs are based on optically thin C^{18}O data. We suggest that these are good candidates for the precursors of rich superclusters like R136 in 30 Dor, which includes more than 10^4 stars in a small volume with a radius of ~1 pc. It is of particular interest to look for even denser gas toward them in higher excitation transitions of the submillimeter region.

5.2. *Density and Temperature of the Clumps and Implications*

The results of our LVG analysis indicate that clumps are distributed from cool to warm in temperature and from less dense to dense in density. These differences of clump properties in density and temperature show good correspondence with the GMC types based on the star formation activity, as well as with the Hα emission of ionized gas associated with each clump. Clumps in type III GMCs are warm ($T_{\mathrm{kin}} \sim 30$–200 K) and are either dense [$n(\mathrm{H_2}) \sim 10^{3.5}$–$10^5$ cm^{-3}] or less dense [$n(\mathrm{H_2}) \sim 10^3$ cm^{-3}]. Clumps in type II GMCs are either warm ($T_{\mathrm{kin}} \sim 30$–200 K) or cool ($T_{\mathrm{kin}} \sim 10$–30 K) and less dense [$n(\mathrm{H_2}) \sim 10^3$ cm^{-3}]. Clumps in type I GMCs are cool ($T_{\mathrm{kin}} \sim 10$–30 K) and less dense [$n(\mathrm{H_2}) \sim 10^3$ cm^{-3}]. The physical parameters of clumps are

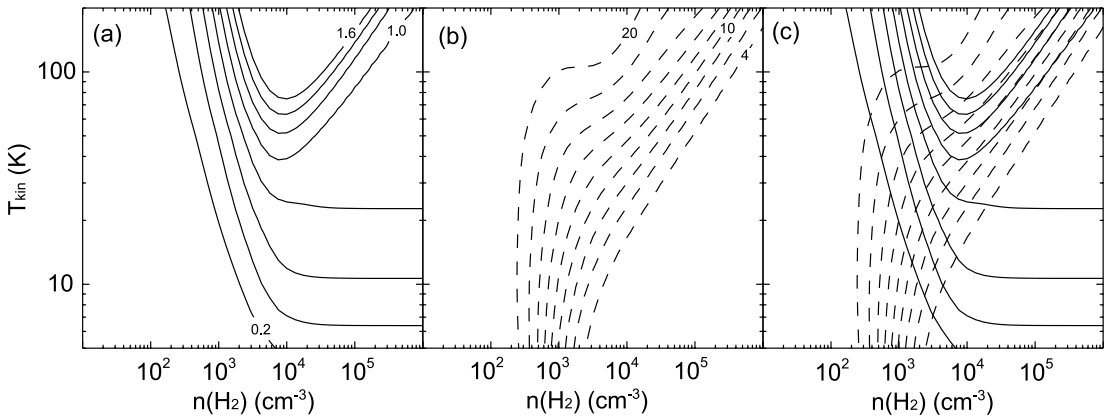

FIG. 19.—Contour plots of LVG analysis for reference. Contours are (*a*) $R_{3-2/1-0}$, (*b*) $R_{12/13}$, and (*c*) $a + b$. Here $X(\mathrm{CO}) = 3 \times 10^{-6}$, $dv/dr = 1.0$ km s^{-1} pc^{-1}, and the abundance ratio of ^{12}CO/^{13}CO is 25.

TABLE 5

SUMMARY OF LVG AND MEAN ESCAPE PROBABILITY ANALYSES

				$R_{12/13}$		This Work		J98		H99		B05 SC		B05 CDC		B05 HTC		K06	
Region	No.	dv/dr (km s^{-1} pc^{-1})	$R_{3-2/1-0,\mathrm{clump}}$	Value	Ref.	$n(H_2)$ (cm^{-3})	T_{kin}	$n(H_2)$ (cm^{-3})	T_{kin}	$n(H_2)$ (cm^{-3})	T_{kin}	$n(H_2)$ (cm^{-3})	T_{kin}	$n(H_2)$ (cm^{-3})	T_{kin}	$n(H_2)$ (cm^{-3})	T_{kin}	$n(H_2)$ (cm^{-3})	T_{kin}
(1)	(2)	(3)	(4)	(5)	(6)	(7)	(8)	(9)	(10)	(11)	(12)	(13)	(14)	(15)	(16)	(17)	(18)	(19)	(20)
30 Dor	1	0.9	1.4	11.5	J98	3×10^3 to 3×10^5	>50	$10^{4.5}$	40–80	1×10^5	50							$10^{4.3}$	100
	4	0.5	1.3	17.7	J98	1×10^3 to 1×10^5	>60	$10^{4.5}$	>20										
N159	1	0.9	1.1	8.6	J98	3×10^3 to 8×10^5	>30	$10^{4.5}$	16–23	3×10^5	25	10^3	150	10^5	20	10^2	100		
	2	0.5	1.1	11.6	J98	1×10^3 to 3×10^5	>40												
	4	0.4	0.7	8.5	J98	1×10^3 to 6×10^3	20–60			1×10^5	10								
N166	1	0.3	0.6	10.5	G02	5×10^2 to 2×10^3	25–150												
	3	0.3	0.6	12.6	G02	3×10^2 to 2×10^3	>30												
	4	0.4	0.6	16.2	G02	4×10^2 to 2×10^3	>40							10^4	20	10^2 to 10^3	30–60		
N206	1	0.5	0.8	14.1	This work	5×10^2 to 3×10^3	>35												
	2	0.4	0.5	9.8	This work	6×10^2 to 2×10^3	20–80												
N206D	1	0.3	0.5	4.8	This work	1×10^3 to 3×10^3	10–20												
GMC 225	1	0.2	0.4	6.6	This work	5×10^2 to 2×10^3	15–20												
	3	0.3	0.4	6.7	This work	7×10^2 to 2×10^3	10–40												

NOTES.—Cols. (7) and (8): Results of LVG analysis. Cols. (9)–(20): Results of previous studies, including both LVG and mean escape probability analyses.

REFERENCES.—(J98) Johansson et al. 1998; (G02) Garay et al. 2002; (H99) Heikkilä et al. 1999; (B05 SC) "Single-component fit" in Bolatto et al. 2005; (B05 CDC, B05 HTC) "Cold Dense Component" and "Hot Tenuous Component," respectively, of the "Dual-component fit" in Bolatto et al. 2005; (K06) Kim 2006.

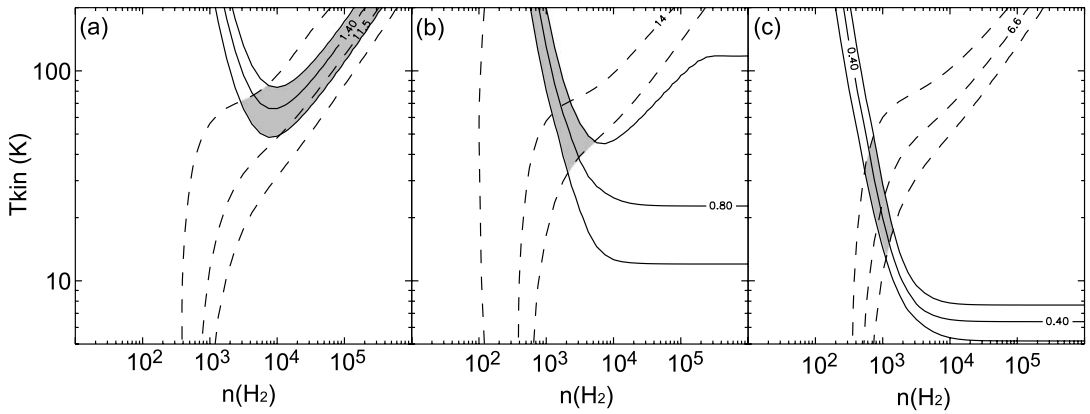

FIG. 20.—Contour plots of LVG analysis of three clumps: (*a*) 30 Dor No. 1, (*b*) N206 No. 1, and (*c*) GMC 225 No. 1. The vertical axis is kinetic temperature $T_{\rm kin}$, and the horizontal axis is molecular hydrogen density $n(\rm H_2)$. Solid lines indicate $R_{3-2/1-0,\rm clump}$, and dashed lines indicate $R_{12/13}$. Hatched areas are the regions in which these two ratios overlap within intensity calibration errors of 20% and uncertainty due to a possible variation of ^{12}CO/^{13}CO abundance ratio from 20 to 30.

generally correlated with the star formation activity of GMCs and can perhaps be interpreted in terms of evolutionary effects.

Our interpretation is that differences of clump density and temperature represent an evolutionary sequence of GMCs in terms of density increase leading to star formation; type I/II GMCs are at a young phase of star formation where density has not yet reached high enough values to cause active massive star formation, and type III GMCs represent the later phase where the average density is higher, including both high- and low-density subtypes. The high-density clumps in type III GMCs show high $R_{3-2/1-0,\rm clump}$ of 1.0–1.5 and are associated with strong Hα flux, while the low-density clumps in type III GMCs show low $R_{3-2/1-0,\rm clump}$ of 0.5–1.0 with weak Hα flux.

We suggest two alternative ideas to explain the density difference of the clumps in type III GMCs; one is that density is being enhanced by shock compression driven by H II regions, and the other is that gravitational condensation of each clump plays a role in the density increase. The former may be difficult because the shock front may occupy a small volume that is likely missed with the present 5 pc beam. It seems thus favorable that the latter scenario is working mainly to enhance density.

The present study, which resolved the smaller clumps in GMCs at 5–10 pc scales, indicates that the clumps may have physical properties affected by local properties such as the Hα distribution. It should be interesting to investigate the variations among these internal clumps and their relation to star formation.

5.3. *FUV Heating of the Molecular Gas in the LMC*

The present findings that the $R_{3-2/1-0,\rm clump}$ is well correlated with Hα flux suggest that the heating of molecular gas by far-ultraviolet (FUV) photons may be effective in the LMC where the dust opacity is lower and the FUV intensity is higher than in the Milky Way. The molecular gas in the Milky Way is mainly heated by cosmic-ray protons of $\sim$100 MeV as discussed by a number of authors, although the surface layers of molecular clouds with small visual extinctions at A_V around a few magnitudes or less may be dominated by the FUV heating (e.g., Kaufman et al. 1999). Some authors have made detailed calculations of gas heating and cooling under the effects of FUV radiation fields (Kaufman et al. 1999). We try to present a picture that can be applied to the present results below.

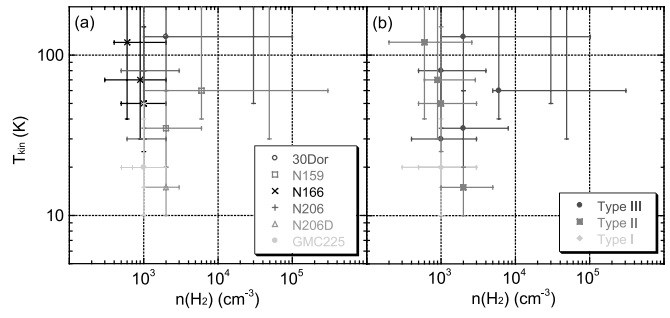

FIG. 21.—Plot of LVG results. The vertical axis is kinetic temperature, $T_{\rm kin}$, and the horizontal axis is molecular hydrogen density $n(\rm H_2)$. [*See the electronic edition of the Supplement for a color version of this figure.*]

First, the gas temperature is determined through the balance between the cooling and heating. According to Table 4 in Goldsmith & Langer (1978) the total cooling rate is $6.8\times10^{-27}T^{2.2}$ ergs cm^{-3} s^{-1} for $X(\rm CO)/(dv/dr) = 4\times10^{-5}$ and $n(\rm H_2) = 10^3$ cm^{-3}. In the 30 Dor region, since $X(\rm CO)/(dv/dr) = 3\times10^{-6}/0.8 = 3.75\times10^{-6}$ and this value is 10 times lower than the value used in Goldsmith & Langer (1978), $n(\rm H_2)=10^4$ cm^{-3} can be read 10^3 cm^{-3}; then the cooling rate is estimated as 1.7×10^{-22} ergs cm^{-3} s^{-1} for $T = 100$ K. This value is a factor 2–3 smaller than that of Galactic clouds with $n(\rm H_2) = 10^4$ cm^{-3} and $T = 50$ K.

We assume that the heating by cosmic-ray electrons is not important in the LMC. This assumption is not directly confirmed, but it is consistent with the low nonthermal fraction of the LMC's radio continuum emission (e.g., Hughes et al. 2006) and studies that suggest that a significant fraction of cosmic-ray electrons are able to escape from low-luminosity galaxies (e.g., Bell 2003; Skillman & Klein 1988).

The FUV flux (G_0) is estimated as 3500 for 30 Doradus (Bolatto et al. 1999; Poglitsch et al. 1995; Werner et al. 1978; Israel & Koornneef 1979) and 300 for N159 (Bolatto et al. 1999; Israel et al. 1996; Israel & Koornneef 1979). In Orion, it is estimated as 25 (Bolatto et al. 1999; Stacey et al. 1993). The FUV flux in the LMC is larger than that in the Milky Way.

Photodissociation region (PDR) models are calculated by Kaufman et al. (1999) that incorporate the chemical and physical processes that form and destruct atoms or molecules, as well as ionization effects. Figure 1 of Kaufman et al. (1999) shows the kinetic temperature for a molecular gas layer with density of n (cm^{-3}) under FUV flux of G_0 at the surface. PDR surface temperatures are estimated as listed in Table 7. These indicate that temperature becomes as high as 100–300 K on the PDR surface under the conditions of the clumps in type III GMCs in the LMC. These temperatures are basically consistent with the temperatures of the warm clumps in the present sample.

TABLE 6
EFFECT OF X(CO)

X(CO) Conditions	Parameter	30 Dor No. 1	N159 No. 1	N159 No. 4
		This Work		
Uniform X(CO).....	X(CO)	3×10^{-6}	3×10^{-6}	3×10^{-6}
	$n(H_2)$ (cm^{-3})	3×10^{3} to 3×10^{5}	3×10^{3} to 8×10^{5}	1×10^{3} to 6×10^{3}
	T_{kin} (K)	>50	>30	20–60
Different X(CO)	X(CO)	1×10^{-6}	1×10^{-5}	3×10^{-6}
	$n(H_2)$ (cm^{-3})	6×10^{3} to 1×10^{6}	2×10^{3} to 2×10^{5}	1×10^{3} to 6×10^{3}
	T_{kin} (K)	>35	>45	20–60
		Heikkilä et al. (1999)		
Different X(CO)	X(CO)	1.4×10^{-6}	1.2×10^{-5}	4.6×10^{-6}
	$n(H_2)$ (cm^{-3})	1×10^{5}	3×10^{5}	1×10^{5}
	T_{kin} (K)	50	25	10

Generally speaking, at a scale of ~10 pc, $T_{kin} \sim 100$ K seems to be higher than the kinetic temperatures typical in Milky Way GMCs, where the Milky Way values are usually derived from the ^{12}CO($J = 1$–0) emission only (e.g., η Car $T_{kin} \sim 50$ K by Yonekura et al. 2005). This suggests that the heating of molecular clouds may be stronger in the LMC than in the Milky Way and the molecular temperature may be higher. If this is correct, the lower metallicity, resulting in lower extinction, is the basic cause for the higher temperature in addition to the stronger FUV field in the LMC. We note in the end that this higher temperature in the molecular gas possibly leads to an increase of the Jeans mass of molecular clumps, which may favor the formation of rich superclusters in the LMC. This is consistent with the higher mass of the molecular clumps, which may represent precursors of the clusters.

The present work has undertaken to sample six GMCs (seven regions) to have a uniform determination of the density and temperature in the LMC. The number of GMCs is still limited to 6 among ~300 detected with NANTEN. We should make more efforts to collect appropriate data sets in the submillimeter wavelengths to improve our understanding of the cloud properties.

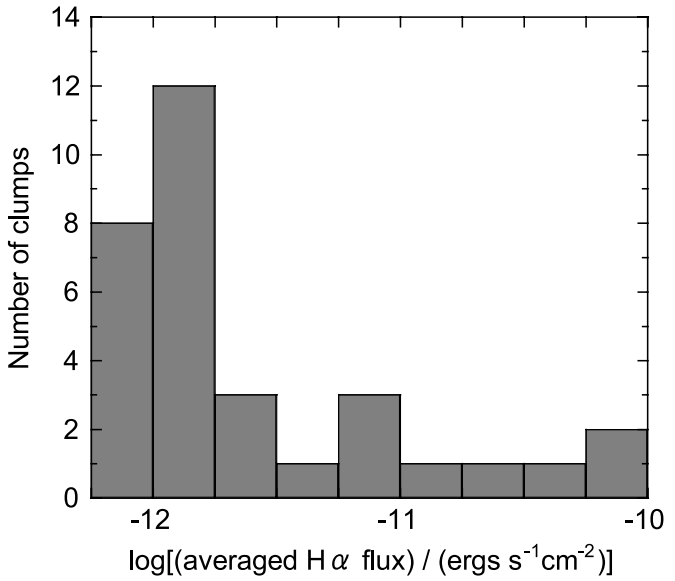

FIG. 22.—Histogram of clump-averaged Hα flux. Background level is nearly 10^{-12} ergs s^{-1} cm^{-2}.

NANTEN2, ASTE, and others will certainly be powerful in achieving this goal.

6. SUMMARY

We summarize the results as follows.

1. We have used the ASTE 10 m telescope to obtain the distribution of ^{12}CO($J = 3$–2) emission at 345 GHz toward six GMCs (seven regions) in the LMC. We have identified 32 clumps in these GMCs at ~5 pc resolution. The radius, line width, and virial mass are estimated as 1.1–12.4 pc (7 pc), 4.0–12.8 km s^{-1} (7 km s^{-1}), and 4.6×10^3 to 2.2×10^5 $M_\odot$ (6×10^4 $M_\odot$), respectively, with the average values in the parenthesis.

2. We have compared the present results with LVG radiative line transfer calculations in order to obtain the density and temperature estimated for the 13 clumps using $R_{3-2/1-0,clump}$ and $R_{12/13}$ at 45″ resolution. The clumps are distributed from cool (~10–30 K) to warm (more than ~30–200 K) and from less dense [$n(H_2) \sim 10^3$ cm^{-3}] to dense [$n(H_2) \sim 10^{3.5}$–10^5 cm^{-3}].

3. The Hα flux toward these clumps is well correlated with the ^{12}CO($J = 3$–2)/^{12}CO($J = 1$–0) ratio, $R_{3-2/1-0,clump}$, and clumps with Hα fluxes greater than 10^{-11} ergs s^{-1} cm^{-2} have large $R_{3-2/1-0,clump}$ of ~1.5. The ^{12}CO($J = 1$–0) data were taken with the SEST 15 m and Mopra 22 m telescopes.

4. The typical mass of the molecular clumps ranges from 5×10^3 to 2×10^5 $M_\odot$ with radii of 1–12 pc. Of all of our objects, N159 No. 1 or W shows the strongest concentration of mass of $\sim 7 \times 10^4$ $M_\odot$ within a radius of ~5 pc. We suggest that these are good candidates for the precursors of rich superclusters like R136 in 30 Dor.

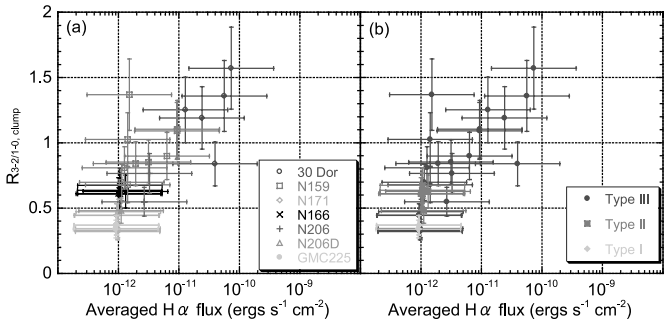

FIG. 23.—Plots of $R_{3-2/1-0,clump}$ as a function of clump-averaged Hα flux by (*a*) region and (*b*) GMC type. [*See the electronic edition of the Supplement for a color version of this figure.*]

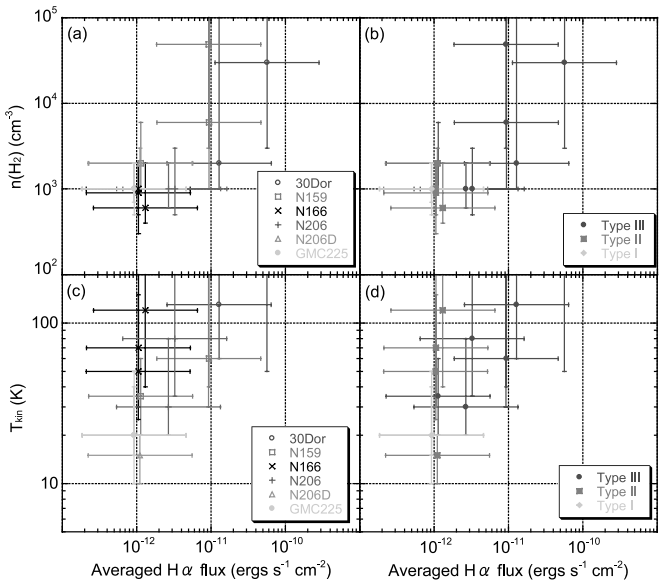

FIG. 24.—Plots of physical properties as a function of clump-averaged Hα flux. (*a*) $n(H_2)$ by region. (*b*) $n(H_2)$ by GMC type. (*c*) T_{kin} by region. (*d*) T_{kin} by GMC type. [*See the electronic edition of the Supplement for a color version of this figure.*]

5. We suggest that differences of clump properties represent an evolutionary sequence of GMCs in terms of density increase leading to star formation. Type I/II GMCs are at a young phase of star formation where density has not yet reached high enough values to cause active massive star formation, and type III GMCs represent the later phase where the average density is higher, including both high- and low-density subtypes.

6. The high kinetic temperature correlated with Hα flux suggests that FUV heating is dominant in the molecular gas of the LMC. The low fraction of nonthermal radio continuum emission and calculations of PDR models support this suggestion. Furthermore, the high temperature in the molecular gas possibly leads to an increase of the Jeans mass of molecular clumps, which may favor the formation of rich superclusters.

TABLE 7

ESTIMATED PDR SURFACE TEMPERATURES

Region (1)	n (cm^{-3}) (2)	G_0 (3)	T_s [a] (K) (4)	References (5)
30 Dor.....	10^4	3500	300	1, 2, 3, 4
N159.....	10^4	300	100	1, 4, 5

NOTES.—Col. (1): Regions. Col. (2): Gas density. Col. (3): FUV flux in units of local interstellar value; 1.6×10^{-3} ergs cm^{-2} s^{-1}. Col. (4): Derived PDR surface temperature of the atomic gas. Col. (5): References of FUV flux.

[a] Estimation is done by using Fig. 1 of Kaufman et al. 1999.

REFERENCES.—(1) Bolatto et al. 1999; (2) Poglitsch et al. 1995; (3) Werner et al. 1978; (4) Israel & Koornneef 1979; (5) Israel et al. 1996.

A part of this study was financially supported by MEXT Grants-in-Aid for Scientific Research on Priority Area (15071202 and 15071203) and by JSPS (No. 14102003, core-to-core program 17004, and No. 18684003). T. M. is supported by JSPS Research Fellowships for Young Scientists. M. R. and S. N. are supported by the Chilean Center for Astrophysics FONDAP 15010003. S. K. was supported in part by the Korea Science and Engineering Foundation (KOSEF) under a cooperative agreement with the Astrophysical Research Center of the Structure and Evolution of the Cosmos (ARCSEC).

ASTE is a joint project between Japan and Chile. The telescope is operated by the ASTE team, including NAOJ, University of Tokyo, Nagoya University, Osaka Prefecture University, and Universidad de Chile. We are grateful to all the members of the ASTE team.

APPENDIX A

COMPLETE LVG RESULTS OF ALL CLUMPS

Figures 25–37 show the complete LVG results described in § 4.2. We present all cases: X(CO) of (*a*) 1×10^{-6}, (*b*) 3×10^{-6}, and (*c*) 1×10^{-5} for 13 clumps.

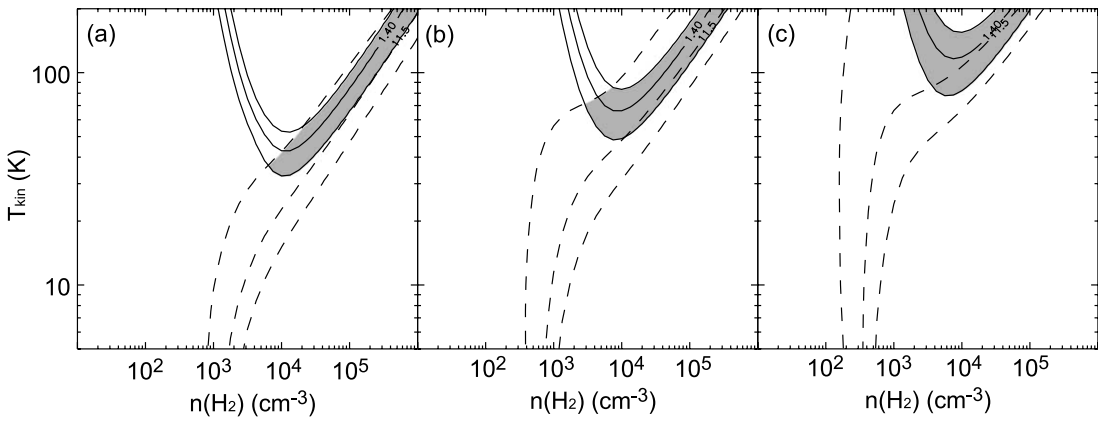

FIG. 25.—Contour plots of LVG analysis of 30 Dor No. 1. The vertical axis is kinetic temperature, T_{kin}, and the horizontal axis is molecular hydrogen density, $n(H_2)$. Solid lines represent $R_{3-2/1-0,clump}$, and dashed lines represent $R_{12/13}$. Hatched areas are the regions in which these two ratios overlap within intensity calibration errors and uncertainty due to a possible variation of $^{12}CO/^{13}CO$ abundance ratio. Here X(CO) = (*a*) 1×10^{-6}, (*b*) 3×10^{-6}, and (*c*) 1×10^{-5}.

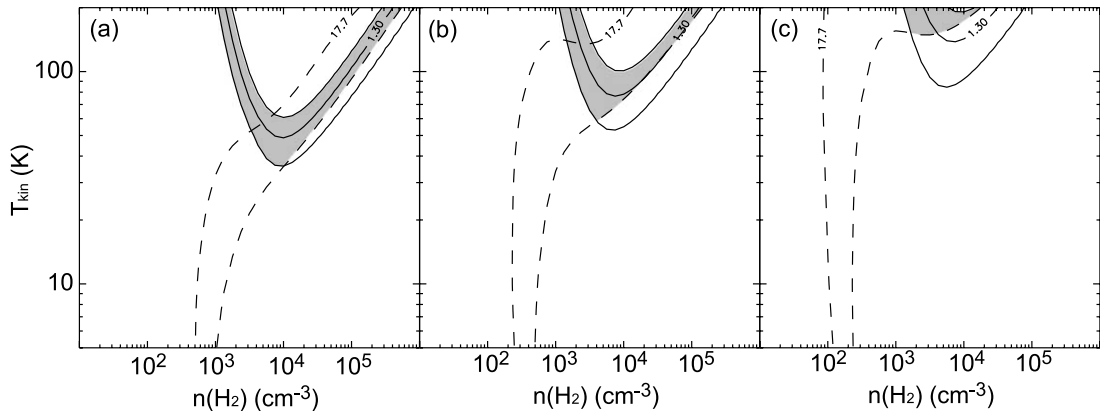

FIG. 26.— Same as Fig. 25, but for 30 Dor No. 4.

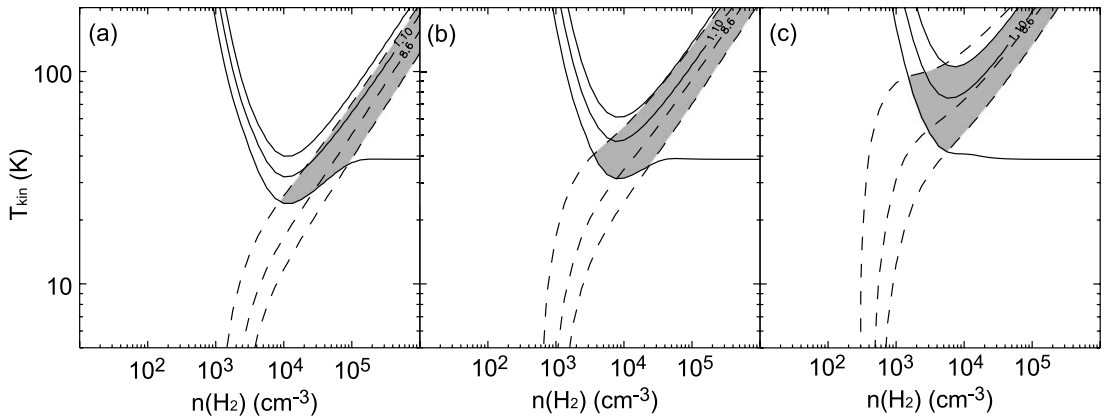

FIG. 27.— Same as Fig. 25, but for N159 No. 1.

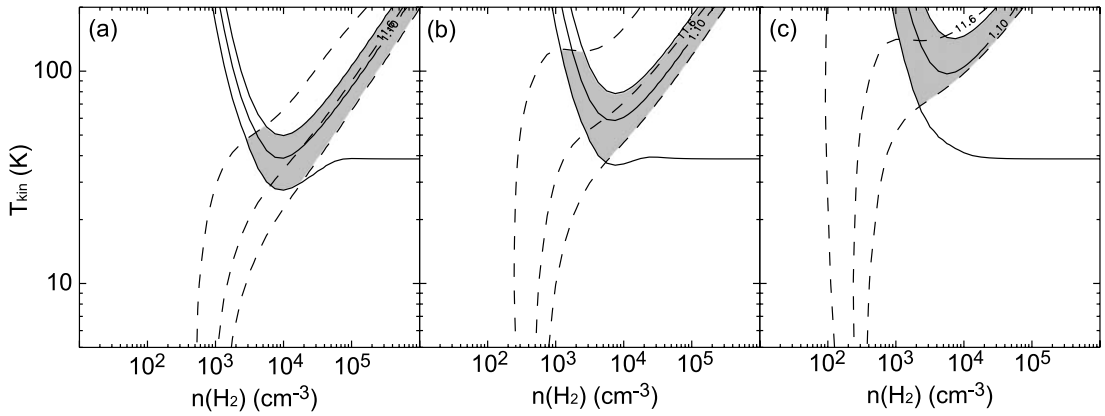

FIG. 28.— Same as Fig. 25, but for N159 No. 2.

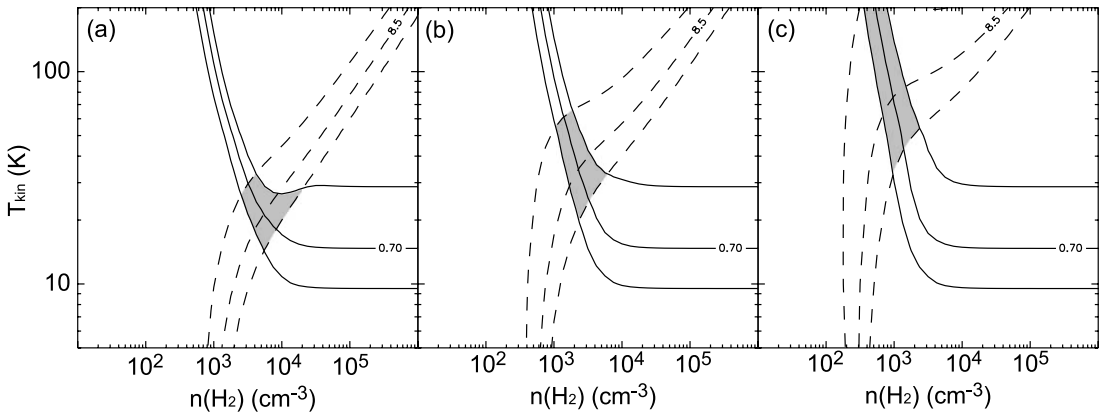

FIG. 29.—Same as Fig. 25, but for N159 No. 4.

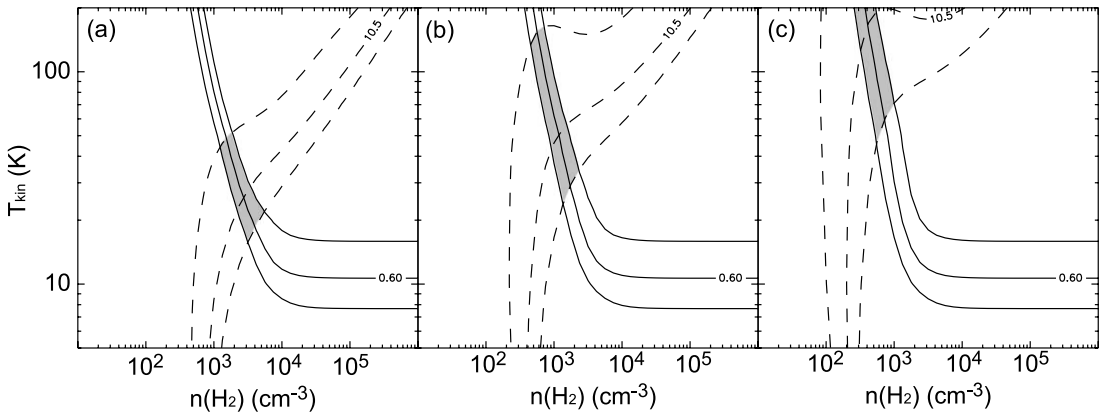

FIG. 30.—Same as Fig. 25, but for N166 No. 1.

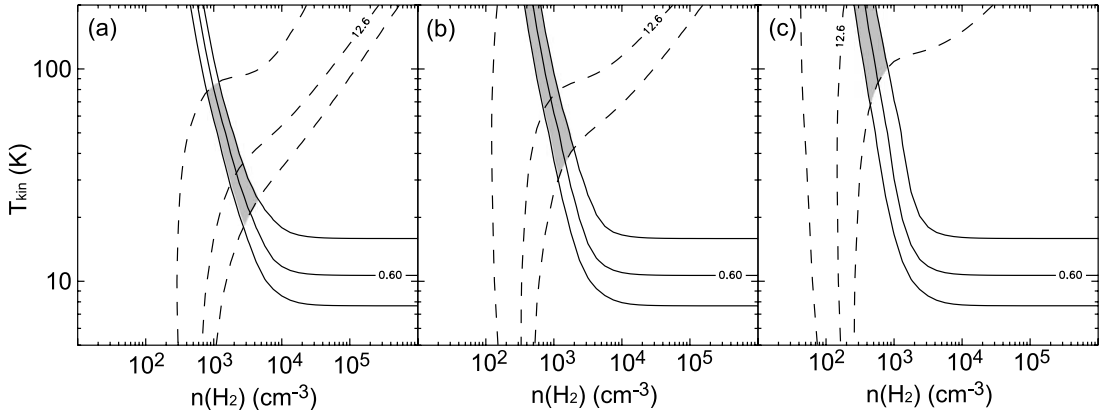

FIG. 31.—Same as Fig. 25, but for N166 No. 3.

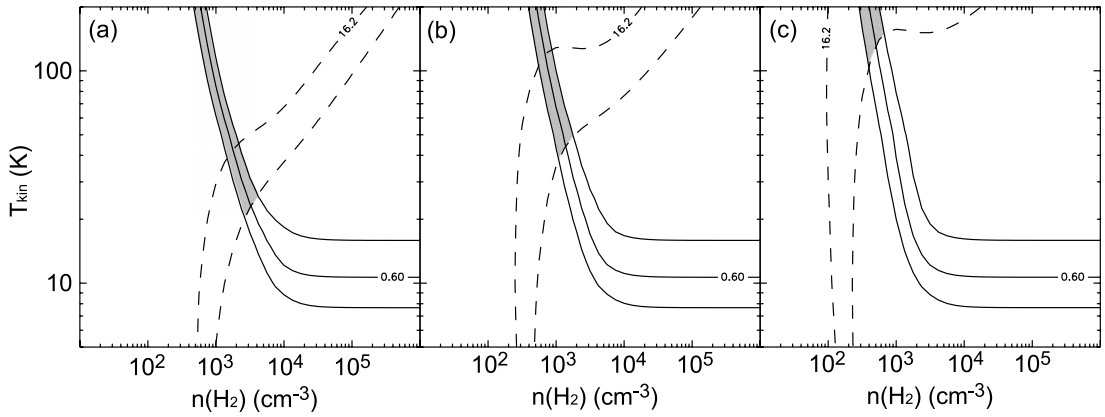

FIG. 32.—Same as Fig. 25, but for N166 No. 4.

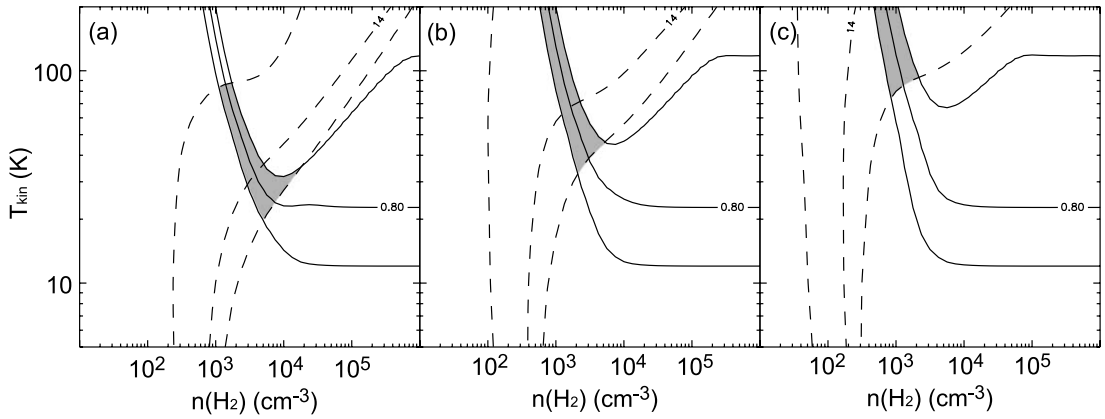

FIG. 33.—Same as Fig. 25, but for N206 No. 1.

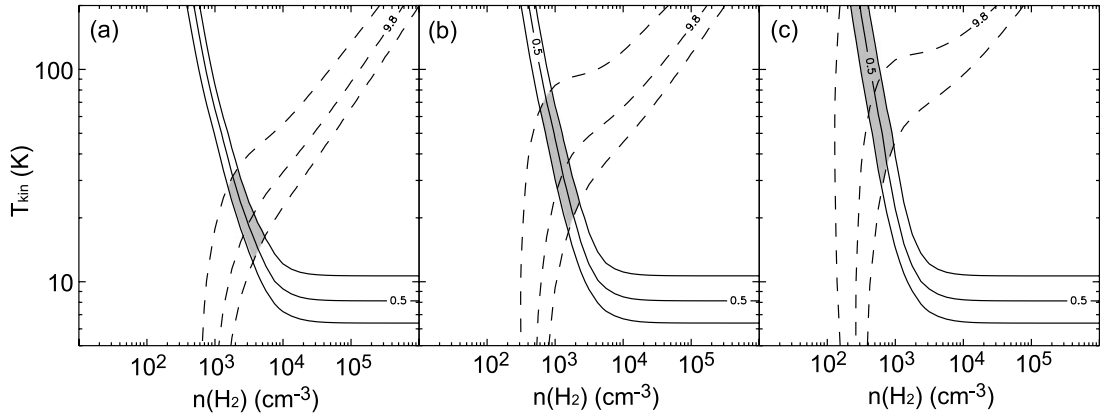

FIG. 34.—Same as Fig. 25, but for N206 No. 2.

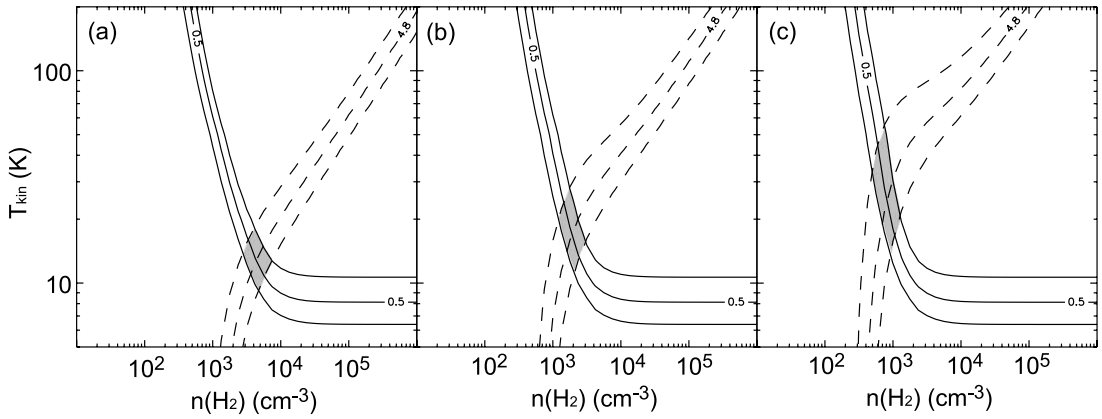

FIG. 35.— Same as Fig. 25, but for N206D No. 1.

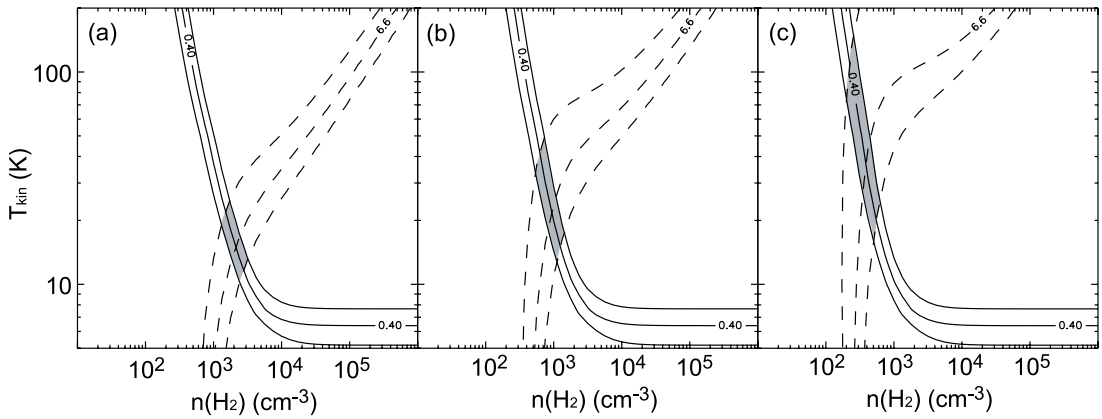

FIG. 36.— Same as Fig. 25, but for GMC 225 No. 1.

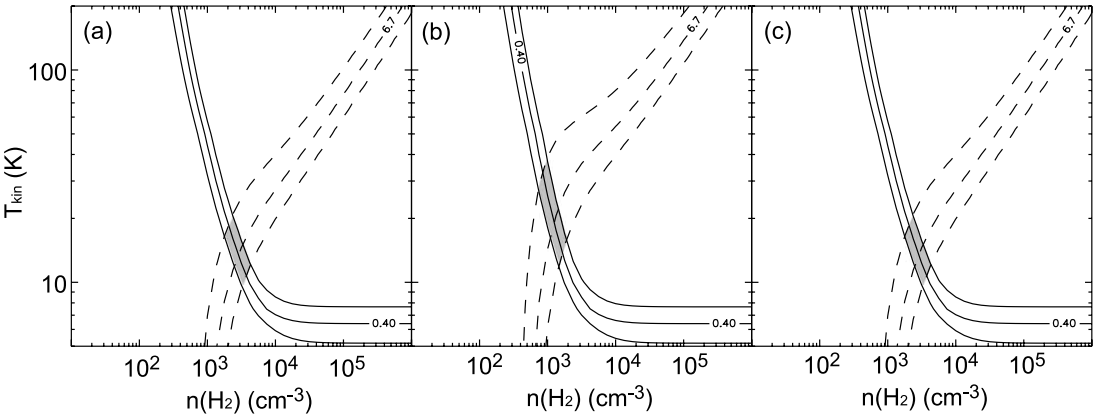

FIG. 37.— Same as Fig. 25, but for GMC 225 No. 3.

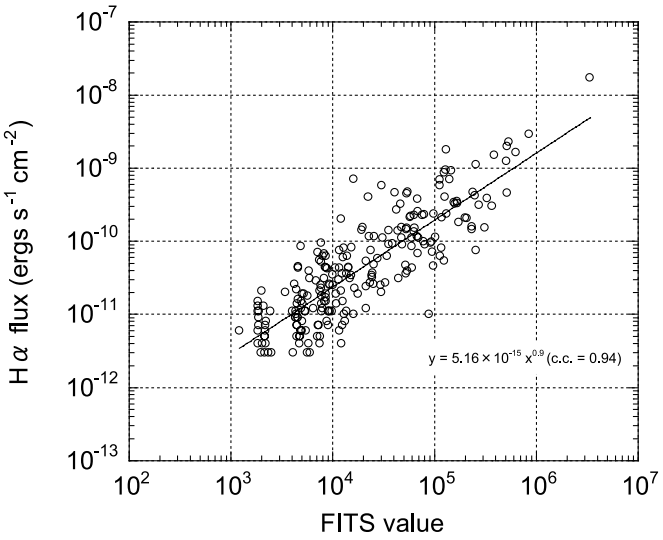

FIG. 38.—Plot of relation between integrated Hα flux and FITS value. The solid line represents the least-squares fit.

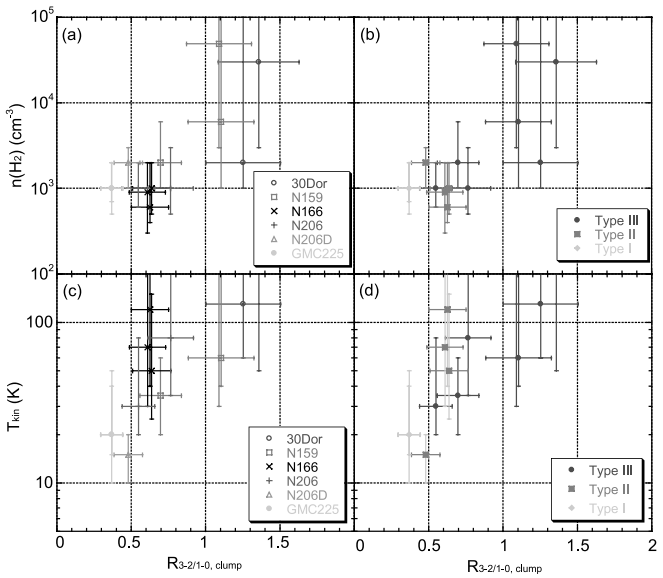

FIG. 39.—Plots of physical properties as a function of $R_{3-2/1-0,\mathrm{clump}}$. (*a*) $n(\mathrm{H_2})$ by region. (*b*) $n(\mathrm{H_2})$ by GMC type. (*c*) T_{kin} by region. (*d*) T_{kin} by GMC type. [*See the electronic edition of the Supplement for a color version of this figure.*]

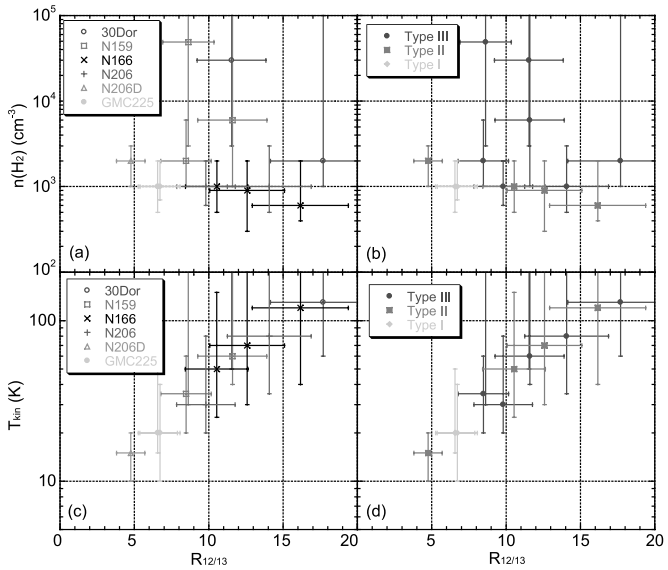

FIG. 40.—Same as Fig. 39, but as a function of $R_{12/13}$. [*See the electronic edition of the Supplement for a color version of this figure.*]

APPENDIX B

Hα FLUX

We here describe the method of scaling data values in the FITS cube (Hα image in Kim et al. [1999], hereafter "Kim's FITS"). The data values in Kim's FITS are not flux scale, and the calibration is needed for quantitative comparison with CO clouds and $R_{3-2/1-0}$. The procedure is as follows. (1) Sum up the data values of Kim's FITS inside apertures, which are listed in Kennicutt & Hodge (1986) for each listed H II region. (2) Plot cataloged values of Hα flux in Kennicutt & Hodge (1986) as a function of summed values derived in step 1. They are well fitted by a power function of $y = 5.16 \times 10^{-15} x^{0.9}$ (c.c. = 0.94; Fig. 38). (3) Convert data values of Kim's FITS to Hα flux scale (ergs s^{-1} cm^{-2}) using the function derived above.

APPENDIX C

LVG RESULTS IN THE OTHER PLANES

C1. PHYSICAL PROPERTIES: $R_{3-2/1-0,\mathrm{clump}}$ (FIG. 39)

The density plots (Figs. 39*a* and 39*b*) show that higher $R_{3-2/1-0,\mathrm{clump}}$ (>1.0) correspond to higher densities of 10^3–10^5 cm^{-3}, while lower $R_{3-2/1-0,\mathrm{clump}}$ (<1.0) correspond to lower densities of around 10^3 cm^{-3}. The temperature plots (Figs. 39*c* and 39*d*) show that higher $R_{3-2/1-0,\mathrm{clump}}$ (>0.5) correspond to higher temperatures of >30 K, while lower $R_{3-2/1-0,\mathrm{clump}}$ (<0.5) correspond to lower temperatures of <30 K.

Then, roughly speaking, we can say that clumps with $R_{3-2/1-0,\mathrm{clump}}$ lower than 0.5 have lower densities of around 10^3 cm^{-3} and lower temperatures of <30 K, clumps with $R_{3-2/1-0,\mathrm{clump}}$ of 0.5–1.0 have lower density around 10^3 cm^{-3} and higher temperatures of >30 K, and clumps with $R_{3-2/1-0,\mathrm{clump}}$ higher than 1.0 have higher densities of 10^3–10^5 cm^{-3} and higher temperatures of >30 K, although ratios, densities, and temperatures are with large error bars.

Of course, there are great benefits to using $R_{12/13}$ in LVG analyses. We could not have obtained the above results with only $R_{3-2/1-0}$, as mentioned in § 4.

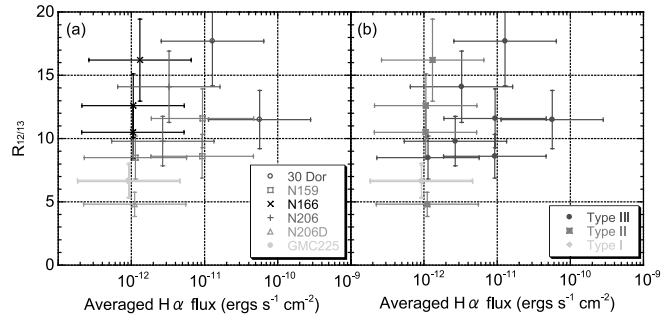

FIG. 41.—Plots of $R_{12/13}$ as a function of clump-averaged Hα flux (*a*) by region and (*b*) by GMC type. [*See the electronic edition of the Supplement for a color version of this figure.*]

The density (Figs. 40*a* and 40*b*) does not show a significant correlation with $R_{12/13}$. The temperature (Figs. 40*c* and 40*d*) shows a good correlation with $R_{12/13}$; that is, higher ratios indicate higher temperatures. Usually, $R_{12/13}$ correspond to density, but in this case, due to the LVG analysis using both $R_{3-2/1-0}$ and $R_{12/13}$, larger $R_{12/13}$ indicate lower density and lower density tends to higher temperature.

C3. $R_{12/13}$-Hα FLUX (FIG. 41)

There is no significant relation between $R_{12/13}$ and Hα flux, in contrast to the case for the $R_{3-2/1-0}$ ratio.

REFERENCES

Bell, E. 2003, ApJ, 586, 794
Bica, E., Clariá, J. J., Dottori, H., Santos, J. F., Jr., & Piatti, A. E. 1996, ApJS, 102, 57
Blitz, L., Fukui, Y., Kawamura, A., Leroy, A., Mizuno, N., & Rosolowsky, E. 2007, in Protostar and Planets V, ed. B. Reipurth, D. Jewitt, & K. Keil (Tucson: Univ. Arizona Press), 81
Bolatto, A. D., Israel, F. P., & Martin, C. L. 2005, ApJ, 633, 210
Bolatto, A. D., Jackson, J. M., & Ingalls, J. G. 1999, ApJ, 513, 275
Burton, M. G., Hill, T., Longmore, N., Purcell, C. R., & Walsh, A. J. 2005, in IAU Symp. 227, Massive Star Birth: A Crossroads of Astrophysics, ed. R. Cesaroni et al. (Cambridge: Cambridge Univ. Press), 157
Castor, J. I. 1970, MNRAS, 149, 111
Dufour, R. J. 1984, in IAU Symp. 108, Structure and Evolution of the Magellanic Clouds, ed. S. van den Bergh & K. S. de Boer (Dordrecht: Reidel), 353
Dufour, R. J., Shields, G. A., & Talbot, R. J., Jr. 1982, ApJ, 252, 461
Ezawa, H., Kawabe, R., Kohno, K., & Yamamoto, S. 2004, Proc. SPIE, 5489, 763
Fukui, Y. 2007, in IAU Symp. 237, Triggered Star Formation in a Turbulent ISM, ed. B. G. Elmegreen & J. Palous (Cambridge: Cambridge Univ. Press), 31
Fukui, Y., Mizuno, N., Yamaguchi, R., Mizuno, A., & Onishi, T. 2001, PASJ, 53, L41
Fukui, Y., et al. 1999, PASJ, 51, 745
———. 2007, ApJ, submitted
Garay, G., Johansson, L. E. B., Nyman, L.-Å., Booth, R. S., Israel, F. P., Kutner, M. L., Lequeux, J., & Rubio, M. 2002, A&A, 389, 977
Goldreich, P., & Kwan, J. 1974, ApJ, 189, 441
Goldsmith, P. F., & Langer, W. D. 1978, ApJ, 222, 881
Heikkilä, A., Johansson, L. E. B., & Olofsson, H. 1999, A&A, 344, 817
Hughes, A., Wong, T., Ekers, R., Staveley-Smith, L., Filipovic, M., Maddison, S., Fukui, Y., & Mizuno, N. 2006, MNRAS, 370, 363
Ikeda, M., et al. 1999, ApJ, 527, L59
Israel, F. P., de Graauw, Th., van de Stadt, H., & de Vries, C. P. 1986, ApJ, 303, 186
Israel, F. P., & Koornneef, J. 1979, ApJ, 230, 390
Israel, F. P., Maloney, P. R., Geis, N., Herrmann, F., Madden, S. C., Poglitsch, A., & Stacey, G. J. 1996, ApJ, 465, 738
Israel, F. P., et al. 2003, A&A, 406, 817
Johansson, L. E. B., Olofsson, H., Hjalmarson, A., Gredel, R., & Black, J. H. 1994, A&A, 291, 89
Johansson, L. E. B., et al. 1998, A&A, 331, 857
Kamazaki, T., et al. 2005, in ASP Conf. Ser. 347, Astronomical Data Analysis Software and Systems XIV, ed. P. Shopbell, M. Britton, & R. Ebert (San Francisco: ASP), 533
Kaufman, M. J., Wolfire, M. G., Hollenbach, D. J., & Luhman, M. L. 1999, ApJ, 527, 795
Kawamura, A., Minamidani, T., Mizuno, Y., Onishi, T., Mizuno, N., Mizuno, A., & Fukui, Y. 2007, in IAU Symp. 237, Triggered Star Formation in a Turbulent ISM, ed. B. G. Elmegreen & J. Palous (Cambridge: Cambridge Univ. Press), 101
Kennicutt, R. C., Jr., & Hodge, P. W. 1986, ApJ, 306, 130
Kim, S. 2006, PASP, 118, 94
Kim, S., Dopita, M. A., Stavely-Smith, L., & Bessell, M. S. 1999, AJ, 118, 2797
Kim, S., Walsh, W., & Xiao, K. 2004, ApJ, 616, 865
Kohno, K. 2005, in ASP Conf. Ser. 344, The Cool Universe: Observing Cosmic Dawn, ed. C. Lidman & D. Alloin (San Francisco: ASP), 242
Kutner, M. L., et al. 1997, A&AS, 122, 255
Ladd, N., Purcell, C., Wong, T., & Robertson, S. 2005, Publ. Astron. Soc. Australia, 22, 62
MacLaren, I., Richardson, K. M., & Wolfendale, A. W. 1988, ApJ, 333, 821
Mizuno, N., et al. 2001, PASJ, 53, 971
Muraoka, K., et al. 2007, PASJ, 59, 43
Poglitsch, A., Krabbe, A., Madden, S. C., Nikola, T., Geis, N., Johansson, L. E. B., Stacey, G. J., & Sternberg, A. 1995, ApJ, 454, 293
Rolleston, W. R. J., Trundle, C., & Dufton, P. L. 2002, A&A, 396, 53
Schöier, F. L., van der Tak, F. F. S., van Dichoeck, E. F., & Black, J. H. 2005, A&A, 432, 369
Skillman, E. D., & Klein, U. 1988, A&A, 199, 61
Sorai, K., et al. 2000, Proc. SPIE, 4015, 86
———. 2001, ApJ, 551, 794
Stacey, G. J., Jaffe, D. T., Geis, N., Genzel, R., Harris, A. I., Poglitsch, A., Stutzki, J., & Townes, C. H. 1993, ApJ, 404, 219
Sun, K., Kramer, C., Ossenkopf, V., Bensch, F., Stutzki, J., & Miller, M. 2006, A&A, 451, 539
Werner, M. W., Becklin, E. E., Gatley, I., Ellis, M. J., Hyland, A. R., Robinson, G., & Thomas, J. A. 1978, MNRAS, 184, 365
Williams, J. P., & Blitz, L. 1998, ApJ, 494, 657
Yamaguchi, R., et al. 2001, PASJ, 53, 985
Yonekura, Y., Asayama, S., Kimura, K., Ogawa, H., Kanai, Y., Yamaguchi, N., Barnes, P. J., & Fukui, Y. 2005, ApJ, 634, 476